bioRxiv preprint doi: https://doi.org/10.1101/2022.03.17.484791; this version posted March 19, 2022. The copyright holder for this preprint (which was not certified by peer review) is the author/funder, who has granted bioRxiv a license to display the preprint in perpetuity. It is made available under aCC-BY-NC-ND 4.0 International license.

A murine model of hnRNPH2-related neurodevelopmental disorder recapitulates clinical features of human disease and reveals a mechanism for genetic compensation of *HNRNPH2*

Ane Korff[1], Xiaojing Yang[1], Kevin O'Donovan[1], Fen Yang[1], Tushar Patni[2], Heather Tillman[3], Abner Gonzalez[4], Yuh Min Chook[4], J. Paul Taylor[1,5]*, and Hong Joo Kim[1]*

*co-senior and co-corresponding authors

[1] Department of Cell and Molecular Biology, St. Jude Children's Research Hospital, Memphis, Tennessee, USA
[2] Department of Biostatistics, St. Jude Children's Research Hospital, Memphis, Tennessee, USA
[3] Department of Pathology, St. Jude Children's Research Hospital, Memphis, Tennessee, USA
[4] Department of Pharmacology, University of Texas Southwestern Medical Center, Dallas, TX, USA
[5] Howard Hughes Medical Institute, Chevy Chase, Maryland, USA

bioRxiv preprint doi: https://doi.org/10.1101/2022.03.17.484791; this version posted March 19, 2022. The copyright holder for this preprint (which was not certified by peer review) is the author/funder, who has granted bioRxiv a license to display the preprint in perpetuity. It is made available under aCC-BY-NC-ND 4.0 International license.

Abstract

Mutations in *HNRNPH2* cause an X-linked neurodevelopmental disorder with a phenotypic spectrum that includes developmental delay, intellectual disability, language impairment, motor function deficits, and seizures. More than 90% of patients with this disorder have a missense mutation within or adjacent to the nuclear localization signal (NLS) of hnRNPH2, although the specific pathogenic consequences of these mutations have not been examined. Here we found that hnRNPH2 NLS mutations result in reduced interaction with the nuclear transport receptor Kapβ2 in vitro and in cultured human cells. These mutations also cause modest accumulation of hnRNPH2 in the cytoplasm, suggesting that mislocalization of the protein might contribute to pathogenesis. We generated two knock-in mouse models with human-equivalent mutations in the endogenous mouse gene *Hnrnph2*, as well as *Hnrnph2* knockout (KO) mice, and subjected them to extensive, deep phenotyping. Mutant knock-in mice displayed a spectrum of phenotypes that recapitulated aspects of the human disorder, including reduced survival in males, craniofacial abnormalities, impaired motor functions, and increased susceptibility to audiogenic seizures. Mutant knock-in male mice developed more severe phenotypes than female mice, likely due to differences in X-chromosome gene dosage. In contrast, two independent lines of *Hnrnph2* KO mice showed no detectable phenotypes. Notably, KO mice had upregulated expression of *Hnrnph1*, a close paralog of *Hnrnph2*, whereas mutant *Hnrnph2* knock-in mice failed to upregulate *Hnrnph1.* Thus, genetic compensation by *Hnrnph1* might be sufficient to counteract the loss of hnRNPH2. These findings suggest that the pathogenesis of *HNRNPH2*-related disorder in humans may be driven by a toxic gain of function or a complex loss of *HNRNPH2* function with impaired compensation by *HNRNPH1.* The carefully phenotyped mutant knock-in mice described here are an important resource for preclinical studies to assess the potential benefit of either gene replacement or therapeutic knockdown of mutant hnRNPH2.

bioRxiv preprint doi: https://doi.org/10.1101/2022.03.17.484791; this version posted March 19, 2022. The copyright holder for this preprint (which was not certified by peer review) is the author/funder, who has granted bioRxiv a license to display the preprint in perpetuity. It is made available under aCC-BY-NC-ND 4.0 International license.

Introduction

De novo pathogenic variants in *HNRNPH2* were identified in 2016 in six unrelated individuals as a novel cause of an X-linked neurodevelopmental disorder whose features include developmental delay, intellectual disability, autism spectrum disorder, tone abnormalities, and seizure (OMIM 300986) (1). Since the initial identification of these mutations, the genotypic and phenotypic spectrum of the disorder has been expanded to include more than 30 individuals with 11 distinct de novo variants (2), as well as several maternally inherited cases (3-5). Although all six individuals in the initial report were female, subsequent studies have identified males carrying missense mutations in *HNRNPH2* associated with a range of overlapping phenotypes (5-7).

More than 90% of individuals with *HNRNPH2*-related neurodevelopmental disorder have a nonsynonymous single nucleotide variant within or adjacent to the nuclear localization signal (NLS) of hnRNPH2, with the two most common missense variants, R206W and R206Q, located within the NLS. Additional variants outside the NLS of hnRNPH2 have been reported in children with similar symptoms. Two of these, at residues 114 and 188, are recurrent, suggesting a potential pathogenic effect (8), whereas additional variants found in single patients are of less clear significance. Notably, individuals with NLS mutations have more severe symptoms than those with variants located outside this region, the latter of which have been reported almost exclusively in males (2, 8, 9).

Rare pathogenic variants in *HNRNPH1*, a close paralog of *HNRNPH2*, have been reported in patients with a syndrome very similar to that observed in *HNRNPH2*-related disorder (10, 11). Half of these variants (4 of 8) are located in the NLS of hnRNPH1. As with mutations in hnRNPH2, patients harboring variants within the NLS of hnRNPH1 display a much more severe phenotype than patients whose variants are located outside the NLS (10, 11). These observations suggest the possibility of a common basis for abnormal neurodevelopment related to impairment of functions shared between hnRNPH1 and hnRNPH2.

hnRNPH2 is a member of the heterogeneous nuclear ribonucleoprotein (hnRNP) family of proteins, which govern various aspects of nucleic acid metabolism including transcription, RNA processing, alternative splicing, mRNA trafficking, mRNA stability, and translation (12). hnRNPH2 is a member of the hnRNP H/F subfamily, which comprises hnRNPH1, hnRNPH2, hnRNPH3, and hnRNPF. As components of a messenger ribonucleoprotein (mRNP) complex, hnRNP H/F proteins shuttle between the nucleus and the cytoplasm and function in both cellular compartments. Nucleocytoplasmic transport of hnRNP F/H proteins is regulated by their proline-tyrosine NLS (PY-NLS), which is located in the center of the protein flanked by two RNA-

bioRxiv preprint doi: https://doi.org/10.1101/2022.03.17.484791; this version posted March 19, 2022. The copyright holder for this preprint (which was not certified by peer review) is the author/funder, who has granted bioRxiv a license to display the preprint in perpetuity. It is made available under aCC-BY-NC-ND 4.0 International license.

recognition motifs (RRMs) (13). In humans, PY-NLSs are recognized for nuclear import by karyopherin β2 (Kapβ2) (14). Deletion of the PY-NLS domain in hnRNPF or mutation of the conserved PY-NLS motif in hnRNPH1 impair nuclear localization of these proteins (13, 14).

Pathogenic mechanisms arising from variants in *HNRNPH2* remain largely unexamined. One recent in vitro study showed deficiencies in nucleocytoplasmic shuttling of hnRNPH2 with NLS mutations (R206W, P209L), as well as alterations in splicing associated with hnRNPH2 R114W (8). However, detailed characterizations of pathogenic mutations have not been reported, nor have faithful models that recapitulate features of the human clinical syndrome. Mechanistic insight into the functional consequences of syndrome-causing mutations and robust, disease-relevant models are essential for therapeutics development.

Here we investigated the consequences of common pathogenic mutations in *HNRNPH2,* focusing on variants within the PY-NLS. Mutant proteins showed reduced interaction with Kapβ2 in vitro and in human cells and modest, but abnormal, accumulation in the cytoplasm when expressed in human cells. Knock-in mice bearing two distinct pathogenic NLS mutations in *Hnrnph2* demonstrated a phenotypic spectrum highly similar to clinical features observed in human patients, including reduced survival in males, craniofacial abnormalities, impaired motor function, and increased susceptibility to audiogenic seizures. In contrast, two independent *Hnrnph2* knockout (KO) mice showed no detectable phenotypes, arguing against a simple loss of hnRNPH2 function as the primary driver of disease. Importantly, *Hnrnph2* KO mice showed significant upregulation of the paralogous gene *Hnrnph1*, whereas knock-in mice did not. Thus, our data suggests the possibility of a toxic gain of function or a complex loss of function driven by a failure in compensation by *Hnrnph1*. This study advances a pathogenic mechanism for *HNRNPH2*-related disorder, suggests a mechanism for genetic compensation of *HNRNPH2*, and provides valuable models for potential use in preclinical studies.

bioRxiv preprint doi: https://doi.org/10.1101/2022.03.17.484791; this version posted March 19, 2022. The copyright holder for this preprint (which was not certified by peer review) is the author/funder, who has granted bioRxiv a license to display the preprint in perpetuity. It is made available under aCC-BY-NC-ND 4.0 International license.

Results

Pathogenic variants alter the nucleocytoplasmic ratio of hnRNPH2 and enhance its recruitment to stress granules. Most hnRNPH2 mutations associated with neurodevelopmental phenotypes are single nucleotide variants located in its PY-NLS, which comprises a central hydrophobic or basic motif followed by the motif R/H/K-X_{2-5}-PY (**Fig. 1a-b**). To examine the impact of disease-causing mutations on the subcellular localization of hnRNPH2, we expressed epitope-tagged wild-type (WT) and variant (R206W, R206Q, and P209L) forms of hnRNPH2 in HeLa cells. Under basal conditions, hnRNPH2 WT was almost exclusively located in the nucleus, consistent with established roles for this protein in nuclear RNA processing steps such as splicing. In contrast, disease-causing variants were found in both the nucleus and cytoplasm (**Fig. 1c-d**). The cytoplasmic accumulation of mutant proteins became more evident when cells were exposed to oxidative stress (0.5 mM $NaAsO_2$), which induced the assembly of cytoplasmic stress granules as marked by eIF3η staining (**Fig. 1c-d**). All disease-causing mutant forms of hnRNPH2, but not hnRNPH2 WT, were associated with stress granules (**Fig. 1c-d**), consistent with previous reports that mutations in the PY-NLS of other hnRNPs interfere with their nuclear import and enhance their incorporation into stress granules (15-17).

We next characterized the subcellular localization of 7 additional variants, 5 of which alter the amino acid sequence within the PY-NLS (R206G, Y210C, R212G, R212T, P213L). The remaining two variants alter the amino acid sequence in RRM3 (D340V) or the C-terminal low complexity domain (LCD; A371Cfs*24), respectively. All hnRNPH2 variants within the PY-NLS showed accumulation of hnRNPH2 protein in the cytoplasm, although the levels of accumulation varied (**Fig. 1e** and **Supplementary Fig. 1**). Importantly, despite mutation-dependent redistribution to the cytoplasm, the majority of hnRNPH2 was still found in the nucleus. Indeed, even with the most severe mutation (P209L), which caused the greatest amount of cytoplasmic accumulation, we estimated that ~75% of hnRNPH2 was found in the nucleus. In contrast, the two non-PY-NLS variants did not show cytoplasmic accumulation of hnRNPH2 (**Fig. 1e** and **Supplementary Fig. 1**); thus cytoplasmic redistribution of hnRNPH2 is not an invariant feature of the neurodevelopmental syndrome. We note that these two non-PY-NLS variants were found in male patients, who are hemizygous and therefore express only mutant hnRNPH2, in contrast to heterozygous female patients who express a mix of WT and mutant protein.

Pathogenic variants impair the interaction between hnRNPH2 and its nuclear transport receptor Kapβ2. Closely paralogous proteins hnRNPH1 and hnRNPF interact with the nuclear

bioRxiv preprint doi: https://doi.org/10.1101/2022.03.17.484791; this version posted March 19, 2022. The copyright holder for this preprint (which was not certified by peer review) is the author/funder, who has granted bioRxiv a license to display the preprint in perpetuity. It is made available under aCC-BY-NC-ND 4.0 International license.

import receptor Kapβ2 via their PY-NLS (13, 14, 18). Given the high degree of identity among hnRNPH1, hnRNPF, and hnRNPH2 (**Fig. 1b**), we predicted that hnRNPH2 would bind to Kapβ2 via its PY-NLS for nuclear import and that disease-causing mutations in the PY-NLS would alter this interaction. To test this hypothesis, we performed GST pulldown assays of GST-tagged WT and mutant (R206W, R206Q, and P209L) versions of the hnRNPH2 PY-NLS (aa 184-210) (**Supplementary Fig. 2a-b**). As a positive control, we used an M9M peptide designed to bind to the PY-NLS binding site of Kapβ2 with an affinity that is ~200-fold stronger than a natural PY-NLS (19). We observed pulldown of Kapβ2 with GST-M9M and GST-hnRNPH2 WT peptide, but not with mutant peptides (**Supplementary Fig. 2b**). When we increased the length of the 5′ and 3′ flanking sequences included in the PY-NLS peptide (aa 179-215, aa 174-220, and aa 169-225), the interaction between Kapβ2 and GST-hnRNPH2 PY-NLS peptide was greatly enhanced (**Supplementary Fig. 2c-e**). Indeed, the longest form of GST-hnRNPH2 PY-NLS WT (aa 169-225) bound Kapβ2 as efficiently as GST-M9M (**Supplementary Fig. 2e**). However, the disease-associated mutant peptides showed reduced interaction with Kapβ2 even when expressed with this larger flanking sequence (**Fig. 2a** and **Supplementary Fig. 2e**). The degree to which the PY-NLS mutations impaired Kapβ2 binding correlated with the degree of cytoplasmic redistribution observed in cells, with P209L having the greatest effect (**Fig. 1c-e** and **Fig. 2a**).

We next expressed full-length hnRNPH2 constructs in cells to test their interaction with Kapβ2 via immunoprecipitation. Consistent with our GST pulldowns, full-length hnRNPH2 WT co-immunoprecipitated efficiently with Kapβ2, whereas all disease-associated mutant proteins showed reduced interaction with Kapβ2 (**Fig. 2b-c**). Notably, PY-NLS mutants (R206W/Q/G, P209L, and Y210C) showed a far greater reduction in Kapβ2 interaction (~50-75%) compared with the non-PY-NLS mutant D340V (**Fig. 2b-c**).

To test the functional consequences of the hnRNPH2-Kapβ2 interaction, we next inhibited Kapβ2 by RNAi-mediated knockdown (**Supplementary Fig. 2f**). Expression of siRNA targeting *KPNB2* (also known as *TNPO1*) resulted in ~90% decrease in Kapβ2 protein levels, increased cytoplasmic localization of endogenous hnRNPH protein, and increased association of hnRNPH with stress granules as assessed by staining with the stress granule marker G3BP1 (**Fig. 2d** and **Supplementary Fig. 2f**). We observed a similar result with overexpression of mCherry-M9M peptide, which caused both endogenous hnRNPH and hnRNPA1 to accumulate in the cytoplasm and form cytoplasmic puncta (**Fig. 2e**). These results support the hypothesis that disease-associated PY-NLS mutations impair the ability of hnRNPH2 to bind Kapβ2, thereby diminishing nuclear import of hnRNPH2 and leading to cytoplasmic accumulation.

bioRxiv preprint doi: https://doi.org/10.1101/2022.03.17.484791; this version posted March 19, 2022. The copyright holder for this preprint (which was not certified by peer review) is the author/funder, who has granted bioRxiv a license to display the preprint in perpetuity. It is made available under aCC-BY-NC-ND 4.0 International license.

hnRNPH2 P209L and R206W mice, but not KO mice, have reduced survival and body weight. Like human *HNRNPH2*, the mouse *Hnrnph2* gene is located on the X chromosome. Human hnRNPH2 and mouse hnRNPH2 have 99% identity; both are 449 amino acids in length, with conservative differences in the identity of only 4 amino acids (<1%), and the PY-NLS motif is perfectly conserved between the two species (**Supplementary Fig. 3**). To investigate the effects of mutations on normal hnRNPH2 function and to model the pathogenicity of mutant hnRNPH2, we generated mouse models by homologous knock-in of the human hnRNPH2 R206W or P209L mutations into mouse *Hnrnph2*. To this end, we substituted two conserved C nucleotides at positions 833 and 835 with T and G, respectively (c.833 C > T and c.835 C > G) for the R206W mutation, and the C nucleotide at position 842 with T (c.842 C > T) for the P209L mutation (**Fig. 3a-b** and **Supplementary Fig. 4a)**. While generating these knock-in mouse lines, we also serendipitously obtained a KO line in which a frameshift caused by an indel generated a premature stop codon, leading to nonsense-mediated mRNA decay (**Fig. 3b** and **Supplementary Fig. 4b-d**). We also obtained a second KO line from the Knockout Mouse Project (KOMP) Repository (C57BL/6NJ-$^{Hnrnph2em1(IMPC)J}$/MmJax, The Jackson Laboratory). These two KO lines differ in two respects: first, in contrast to our KO line, which is driven by an indel with consequent nonsense-mediated decay, the KOMP KO line was generated by a 1451-bp deletion in exon 4, which is predicted to result in a truncated, non-functional transcript. Second, the background strain of our *Hnrnph2* mutant and KO lines is C57BL/6J, whereas the KOMP KO is on a C57BL/6NJ background. Thus, we selected two distinct disease-associated *Hnrnph2* knock-in mouse lines (R206W and P209L) and two distinct *Hnrnph2* KO lines for in-depth phenotypic analysis. Importantly, deep phenotypic analysis of our indel-based KO line and the KOMP KO line yielded equivalent results. For ease of presentation, we include data from our own indel-based KO line (hereafter referred to as KO) in all subsequent figures alongside data from our knock-in lines, whereas all results from the KOMP KO line are compiled in Supplementary Figure 5.

All lines produced viable offspring. All heterozygous females (R206W, P209L, and KO) were born with expected frequencies. In contrast, hemizygous P209L mutant males, but not R206W and KO males, were detected at a lower frequency than predicted by Mendelian laws (64% WT vs. 36% *Hnrnph2*$^{P209L/Y}$), suggesting partial embryonic lethality of males bearing the P209L mutation (**Fig. 3c**). We also crossed heterozygous mutant females to hemizygous mutant males to produce homozygous mutant mice. Again, homozygous females from R206W and KO lines were born close to expected frequencies (**Fig. 3c**). We note that this experiment could not

bioRxiv preprint doi: https://doi.org/10.1101/2022.03.17.484791; this version posted March 19, 2022. The copyright holder for this preprint (which was not certified by peer review) is the author/funder, who has granted bioRxiv a license to display the preprint in perpetuity. It is made available under aCC-BY-NC-ND 4.0 International license.

be performed in the P209L line, as most hemizygous P209L males did not survive long enough to breed. Indeed, less than 15% of *Hnrnph2*$^{P209L/Y}$ males lived to 8 weeks of age (**Fig. 3c-d**). *Hnrnph2*$^{R206W/Y}$ males also had significantly reduced survival up to 8 weeks of age (**Fig. 3d**). In contrast, hemizygous KO males (**Fig. 3d**) as well as heterozygous females from all lines showed no significant changes in survival up to 8 weeks of age (**Supplementary Fig. 6a**). Homozygous females from R206W and KO lines also did not have significantly reduced survival up to 8 weeks, although there was a trend toward reduced survival in *Hnrnph2*$^{R206W/R206W}$ females compared to *Hnrnph2*$^{R206W/X}$ female littermates (**Supplementary Fig. 6b**). These results suggest a dosage-dependent effect of *Hnrnph2* mutation on survival and indicate that the P209L mutation has a more severe effect on survival than R206W, consistent with their respective effects in vitro and in cell lines (**Figs. 1-2**).

To investigate the effects of hnRNPH2 mutations on long-term survival, we monitored a subset of mice for up to 2 years. In this smaller cohort, we found no significant difference in long-term survival between hemizygous males or heterozygous females and WT littermate controls (**Supplementary Fig. 6c**). *Hnrnph2*$^{P209L/Y}$ and *Hnrnph2*$^{R206W/Y}$ males weighed significantly less than their WT littermate controls (**Fig. 3e**). *Hnrnph2*$^{R206W/X}$ females also had significantly reduced body weight compared to littermate controls. *Hnrnph2*$^{P209L/X}$ females tended to weigh less than littermates, but the difference was not significant (**Supplementary Fig. 6d**). Once more, neither male nor female KO mice were significantly different from controls in body weight or long-term survival, suggesting that reduced survival or reduced body weight in knock-in mice likely does not arise from simple loss of hnRNPH2 function.

hnRNPH2 P209L and R206W mice, but not KO mice, have craniofacial abnormalities and increased incidence of hydrocephalus. All human patients with hnRNPH2-related phenotypes have dysmorphic facial features including almond-shaped eyes, short palpebral fissures, a short philtrum, full lower lip, long columella, hypoplastic alae nali, and micrognathia (1). Although most of these patients have unremarkable MRIs, some do present with vertical configuration of the splenium of the corpus callosum, delayed myelination, and decreased cerebellar volume (2). During initial breeding of founders to WT mice, we noticed that in addition to being smaller overall, *Hnrnph2*$^{P209L/Y}$ males, and to a lesser extent *Hnrnph2*$^{R206W/Y}$ males, appeared to have short snouts and wide-set eyes (**Fig. 4a**). To further investigate this phenotype, we performed in vivo μCT and MRI on a cohort of mutant knock-in and KO mice at 6 and 24 weeks of age.

Manual linear measurements of 11 key craniofacial parameters (20) revealed significant

bioRxiv preprint doi: https://doi.org/10.1101/2022.03.17.484791; this version posted March 19, 2022. The copyright holder for this preprint (which was not certified by peer review) is the author/funder, who has granted bioRxiv a license to display the preprint in perpetuity. It is made available under aCC-BY-NC-ND 4.0 International license.

reduction in skull and nose length in *Hnrnph2*$^{P209L/Y}$ males, *Hnrnph2*$^{R206W/Y}$ males, and *Hnrnph2*$^{P209L/X}$ females at 6 weeks of age, as well as a significant increase in interorbital distance in *Hnrnph2*$^{P209L/Y}$ and *Hnrnph2*$^{R206W/Y}$ males (**Fig. 4b-c**). Furthermore, upper jaw length was significantly reduced in *Hnrnph2*$^{P209L/Y}$ males, *Hnrnph2*$^{R206W/Y}$ males, and *Hnrnph2*$^{P209L/X}$ females, in addition to a reduction in lower jaw length in *Hnrnph2*$^{P209L/Y}$ males (**Supplementary Fig. 7a**). Importantly, no changes were seen in *Hnrnph2* KO mice (**Fig. 4c and Supplementary Fig. 7a**). To investigate this craniofacial phenotype more extensively, we used a population-level atlas for the automatic identification of 51 skull landmarks (21), followed by pairwise comparison between all landmarks (**Fig. 4d**). After correction for multiple comparisons, *Hnrnph2*$^{P209L/Y}$ males, *Hnrnph2*$^{R206W/Y}$ males, and *Hnrnph2*$^{P209L/X}$ females had many significant changes in inter-landmark distances, mostly decreased compared to littermate controls, whereas KO mice showed no differences (**Fig. 4d**). As these measures were not normalized, we were concerned that the observed changes were due to a reduction in the overall size of the mutant mice and not a change in craniofacial shape. To address this, we performed Euclidean distance matrix analysis (EDMA) on 3D landmark coordinate data scaled to centroid size (22, 23). EDMA based on all 51 landmarks revealed a significant difference in global skull shape of *Hnrnph2*$^{P209L/Y}$ males, *Hnrnph2*$^{R206W/Y}$ males, and *Hnrnph2*$^{P209L/X}$ females, but not *Hnrnph2* KO mice (**Fig. 4d**). EDMA based on subsets of biologically relevant landmarks (24) showed significant changes in several anatomical regions of *Hnrnph2*$^{P209L/Y}$ males, *Hnrnph2*$^{R206W/Y}$ males, *Hnrnph2*$^{P209L/X}$ females and, to a lesser extent, *Hnrnph2*$^{R206W/X}$ females (**Supplemental Fig. 7b**). In this analysis, the only changes detected in *Hnrnph2* KO mice were slight but significant differences in the neural crest-mesoderm boundary (**Supplemental Fig. 7b**). Results at 24 weeks of age did not differ significantly from those at 6 weeks (data not shown).

hnRNPH2 P209L and R206W mice often had domed heads typically associated with hydrocephalus that develops before ossification of the cranial sutures. Although the C57BL/6J background has a relatively high incidence of hydrocephalus (0.029% at The Jackson Laboratory), the number of mice with pathologically confirmed hydrocephalus suggested an increased incidence in hnRNPH2 P209L and R206W mutant mice, but not in KO mice, compared with WT controls (**Supplementary Fig. 7c**). The cause of hydrocephalus in these mice is unknown, as we found neither evidence of aqueduct blockage (**Supplementary Fig. 7d**), nor abnormal morphology of cilia on ependymal cells lining the dilated ventricles, nor motile ciliary dysfunction in the respiratory system (data not shown (25)). For a more quantitative measurement of the incidence of hydrocephalus in these lines, mice in the MRI cohort were scored as moderate, high, or severely hydrocephalic. Significantly more 6-week-old

bioRxiv preprint doi: https://doi.org/10.1101/2022.03.17.484791; this version posted March 19, 2022. The copyright holder for this preprint (which was not certified by peer review) is the author/funder, who has granted bioRxiv a license to display the preprint in perpetuity. It is made available under aCC-BY-NC-ND 4.0 International license.

Hnrnph2$^{P209L/Y}$ males, as well as 24-week-old *Hnrnph2*$^{P209L/Y}$ males, *Hnrnph2*$^{R206W/Y}$ males, and *Hnrnph2*$^{P209L/X}$ females had at least moderate hydrocephalus compared to WT littermates (**Fig. 4e and Supplementary Fig. 7e**). Neither male nor female *Hnrnph2* KO mice showed increased incidence of hydrocephalus compared to WT littermates (**Fig. 4e and Supplementary Fig. 7c**). Notably, hydrocephalic mice in this cohort did not have obvious doming of the skull, suggesting onset of hydrocephalus after closure of cranial sutures in this group. In agreement with histology, no evidence of aqueduct blockage was detected on MRI (data not shown). Given the MRI abnormalities observed in some hnRNPH2 patients, we performed automated brain parcellation and volumetrics to investigate group differences in regional brain volumes. Automated alignment of MRI images to the DSURQE atlas (26) revealed no significant differences in any of the 356 cortical, white matter, subcortical, or CSF defined regions (data not shown).

Hematoxylin and eosin (H&E) staining also revealed no gross abnormalities in hnRNPH2 P209L (**Supplementary Fig. 8**), R206W, or KO brains (data not shown), apart from the presence of varying degrees of dilatation of the ventricles, which was interpreted as a strain-specific background hydrocephalus lesion. Furthermore, immunohistochemistry with markers for astrocytes (GFAP) and microglia (IBA1) did not reveal any evidence for inflammation in hnRNPH2 P209L (**Supplementary Fig. 8**), R206W or KO brains (data not shown) compared to their WT littermate controls. In addition, Luxol fast blue staining and immunohistochemistry with OLIG2, a specific and universal marker of oligodendrocytes in the brain, did not reveal any changes in central nervous system myelination (**Supplementary Fig. 8** and data not shown). Finally, immunohistochemistry with the neuronal marker NeuN, and immunofluorescence with cortical layer-specific markers SATB2 (layer II-IV), CTIP2 (layer V), and FOXP2 (layer VI) revealed neither significant cell loss nor altered lamination in the visual, somatosensory, or somatomotor cortex (**Supplementary Fig. 9**).

hnRNPH2 P209L and R206W mice, but not KO mice, have impaired motor function. Mice selected for behavioral phenotyping were first subjected to an observational test battery at 8 weeks of age to obtain an initial and broad screen of phenotypes. Using a modified version of the SHIRPA level 1 protocol, a standardized protocol for comprehensive behavioral and functional assessment (27, 28), we found that global abnormality scores were significantly higher in *Hnrnph2*$^{P209L/Y}$ males compared to their WT littermates, whereas all other mutant and KO males and all females did not differ significantly from controls (**Fig. 5a**). When abnormality scores were generated for specific functions tested in SHIRPA, we found that motor function

bioRxiv preprint doi: https://doi.org/10.1101/2022.03.17.484791; this version posted March 19, 2022. The copyright holder for this preprint (which was not certified by peer review) is the author/funder, who has granted bioRxiv a license to display the preprint in perpetuity. It is made available under aCC-BY-NC-ND 4.0 International license.

was significantly impaired in *Hnrnph2*$^{R206W/Y}$ males, *Hnrnph2*$^{P209L/Y}$ males, and *Hnrnph2*$^{P209L/X}$ females compared to WT littermate controls (**Supplementary Fig. 10a**). In addition, SHIRPA scores for autonomic function were significantly increased in hnRNPH2 P209L females and tended to be increased in males compared to WT littermates. However, KO mice did not show an increase in abnormality scores (**Supplementary Fig. 10b**). Scores for sensory and neuropsychiatric functions were not significantly different between *Hnrnph2* mutant or KO mice and their littermate controls (data not shown).

We next tested mice in specific and sensitive tests of motor function, including balance, coordination, and muscle strength. Rotarod performance was significantly impaired in *Hnrnph2*$^{P209L/Y}$ males, *Hnrnph2*$^{R206W/Y}$ males, and *Hnrnph2*$^{P209L/X}$ females compared with WT littermates, whereas all other mutant or KO males and females did not differ significantly from controls (**Fig. 5b**). A similar impairment of balance and coordination was observed for *Hnrnph2*$^{P209L/Y}$ and *Hnrnph2*$^{R206W/Y}$ males in the beam walking test, with significantly increased time to cross (**Supplementary Fig. 10c**), increased number of hind paw slips, and decreased neurological score compared to WT littermate controls (data not shown). Latency to fall from a wire cage top was significantly decreased in *Hnrnph2*$^{P209L/Y}$ and *Hnrnph2*$^{R206W/Y}$ males (**Fig. 5c**) and grip strength was significantly decreased in *Hnrnph2*$^{P209L/Y}$ males (**Supplementary Fig. 10d**). Finally, gait analysis revealed that *Hnrnph2*$^{P209L/Y}$ males had significantly decreased stride length compared to WT littermates (**Fig. 5d**), whereas overlap, front base width, and hind base width were unchanged (data not shown).

hnRNPH2 P209L and R206W mice, but not KO mice, have increased susceptibility to audiogenic seizures. Although the SHIRPA sensory function screen did not reveal abnormalities in *Hnrnph2* mutant or KO mice, hnRNPH2 patients have reported sensory issues including hypo- and hypersensitivity to pain, temperature, touch, and in some cases sound (2). We therefore next tested mice in specific and sensitive tests of sensory function, including visual acuity, olfactory function, and pain perception. We did not find any significant impairment for any of the *Hnrnph2* mutant or KO mice in the optomotor response, hot plate, or scent habituation tests (**Supplementary Fig. 11**). However, we did find a significant increase in audiogenic seizure susceptibility, which has been used as a measure of both sensory hypersensitivity and epilepsy in mouse models of monogenic autism (29, 30). At postnatal day 21, *Hnrnph2*$^{P209L/Y}$ males, *Hnrnph2*$^{R206W/Y}$ males, and *Hnrnph2*$^{P209L/X}$ females had significantly increased incidence and severity of audiogenic seizures (**Fig. 6a-b**). Similarly, *Hnrnph2*$^{R206W/R206W}$ females were also more susceptible to audiogenic seizures compared to *Hnrnph2*$^{R206W/X}$ female littermates (**Fig.**

bioRxiv preprint doi: https://doi.org/10.1101/2022.03.17.484791; this version posted March 19, 2022. The copyright holder for this preprint (which was not certified by peer review) is the author/funder, who has granted bioRxiv a license to display the preprint in perpetuity. It is made available under aCC-BY-NC-ND 4.0 International license.

6b). In contrast, *Hnrnph2* KO mice showed no significant audiogenic seizure behavior (**Fig. 6b**).

Pathogenic variants alter the nucleocytoplasmic ratio of hnRNPH2 in hnRNPH2 P209L and R206W mice. To examine the impact of disease-causing mutations on the subcellular localization of hnRNPH2 in mice, we performed immunoblot analysis on nuclear and cytoplasmic fractions of cortical tissue. Nuclear hnRNPH2 levels were significantly reduced in *Hnrnph2*$^{P209L/Y}$ males and tended to be decreased in *Hnrnph2*$^{R206W/Y}$ males (**Fig. 7a-b**). As we were unable to detect any hnRNPH2 protein in the cytoplasmic fraction of mutants or WT littermate controls by immunoblot (data not shown), we next performed immunofluorescence on brain sections, a technique that is more sensitive than immunoblot. Using an antibody specific for hnRNPH2, we observed cytoplasmic staining in neurons of both R206W and P209L mutants, but not WT littermate controls (**Fig. 7c**). Together, these results suggest that disease-causing mutations modestly alter the subcellular localization of hnRNPH2 in neurons of mice, similar to what we observed for human hnRNPH2 in HeLa cells. Importantly, despite mutations to the PY-NLS, the vast majority of mutant hnRNPH2 is correctly localized in the nucleus of mouse neurons in vivo (**Fig. 7c**), consistent with our observations in HeLa cells (**Fig. 1c-e**).

Expression of *Hnrnph1* is increased in *Hnrnph2* KO mice but not in hnRNPH2 P209L or R206W mice. *Hnrnph1* is the autosomal conserved paralog of *Hnrnph2* and the two genes are believed to play similar and potentially redundant roles in RNA splicing (31). Mutations in *HNRNPH1* are also associated with a neurodevelopmental syndrome identified in boys that is very similar to hnRNPH2-linked phenotypes (10, 11). Given the high degree of homology between the two genes and the possibility of redundancy in function, we tested the expression of *Hnrnph1* in our *Hnrnph2* mutant and KO mice using digital droplet RT-PCR (ddRT-PCR). In the adult cortex, *Hnrnph1* mRNA levels were significantly increased in male *Hnrnph2* KOs, but not in P209L or R206W mutant males (**Fig. 8a**). This increase of *Hnrnph1* mRNA in male *Hnrnph2* KO mice was accompanied by an increase in hnRNPH1 protein levels (**Supplementary Fig. 12a**). In contrast, expression levels of two other members of hnRNP F/H family, *Hnrnpf* and *Hnrnph3*, remained unaltered in both *Hnrnph2* mutant and KO mice (**Supplementary Fig. 12b**). *Hnrnph2* mRNA levels were significantly decreased in male *Hnrnph2* KO mice, as expected for a transcript subject to nonsense-mediated decay, but unchanged in hemizygous P209L or R206W mutant males. Similar trends were observed for both transcripts in female mice, but differences were not statistically significant (**Fig. 8a**).

To explore the possibility that this increase in *Hnrnph1* expression may compensate for

bioRxiv preprint doi: https://doi.org/10.1101/2022.03.17.484791; this version posted March 19, 2022. The copyright holder for this preprint (which was not certified by peer review) is the author/funder, who has granted bioRxiv a license to display the preprint in perpetuity. It is made available under aCC-BY-NC-ND 4.0 International license.

the loss of *Hnrnph2* in KO mice, we investigated the spatiotemporal expression of these two genes. Assessment of the Allen mouse brain atlas revealed that *Hnrnph1* is expressed at high levels across all 12 major regions of the adult mouse brain, whereas *Hnrnph2* expression is detected at low levels in the olfactory areas and cortical subplate only (32). To examine the spatiotemporal expression of these two genes during mouse brain development, we performed ddRT-PCR and in situ hybridization (ISH) on WT C57BL/6J mice at embryonic day 12.5, 14.5, 16.5, and postnatal day 0, 7, 14, and 56. Quantification of the ISH generated an "H-score" reflecting mRNA expression level in the tissue section based on the detection of specific probe signal in cells of interest. In the cortex, *Hnrnph1* was expressed at significantly higher levels than *Hnrnph2* at all time points examined (**Fig. 8b**). Furthermore, whereas *Hnrnph1* mRNA levels decreased significantly after E16.5, *Hnrnph2* mRNA levels did not significantly change over the course of the 7 developmental time points (**Fig. 8b**). ISH on whole brains showed similar results, with the H-score for *Hnrnph1* being significantly higher than that for *Hnrnph2* at all time points except P56. Furthermore, *Hnrnph1* H-scores significantly decreased after E12.5, whereas *Hnrnph2* H-scores remained stable over all time points (**Fig. 8c**). Spatial expression analysis of adult (P56) brains revealed that both *Hnrnph1* and *Hnrnph2* are expressed in similar areas, including regions within the telencephalon, brain stem, and hindbrain, as well as fiber tracts (**Fig. 8d**). A similar pattern of spatiotemporal expression has been reported for hnRNPH1 and hnRNPH2 in human brain (33, 34) and human brain organoids (35) (**Supplementary Fig. 12c-e**). In sum, *HNRNPH1* and *HNRNPH2* show similar spatial and temporal expression patterns in human and mouse brains. *HNRNPH1* is highly expressed during early developmental stages and decreases over time, whereas *HNRNPH2* expression is consistently modest throughout development, suggesting that hnRNPH1 governs early brain developmental processes that are gradually shared with its homolog hnRNPH2 at later and/or post-developmental stages.

For the specific type of mouse brain cells that express *Hnrnph1* and *Hnrnph2*, we turned to publicly available databases. At P7, RNA-seq data indicates that both genes are expressed in all the major cell classes of the brain, including astrocytes, neurons, oligodendrocyte precursor cells, newly formed oligodendrocytes, myelinating oligodendrocytes, microglia, and endothelial cells (36, 37) (**Fig. 8e**). In the adult mouse brain, single-cell RNA-seq (38) has demonstrated that the top 5 expression cell clusters for *Hnrnph1* and *Hnrnph2* show significant overlap, including cells that undergo adult neurogenesis in the striatum, granular neurons in the cerebellum, and Cajal-Retzius neurons in the hippocampus (**Fig. 8f**). Together, these data suggest that *Hnrnph1* and *Hnrnph2* have closely matching expression patterns with regard to

bioRxiv preprint doi: https://doi.org/10.1101/2022.03.17.484791; this version posted March 19, 2022. The copyright holder for this preprint (which was not certified by peer review) is the author/funder, who has granted bioRxiv a license to display the preprint in perpetuity. It is made available under aCC-BY-NC-ND 4.0 International license.

brain regions and cell types. Importantly, as development proceeds, expression of *Hnrnph1* decreases while expression of *Hnrnph2* persists; thus, normal cellular function becomes progressively more dependent on hnRNPH2. These observations support our hypothesis that upregulation of *Hnrnph1* in the setting of *Hnrnph2* KO mice compensates for the functional loss of hnRNPH2.

Discussion

The hnRNP family of proteins has a significant enrichment of de novo variants associated with neurodevelopmental disorders with similar clinical phenotypes and potentially shared molecular pathogenesis (39). Mutations in *HNRNPH2* and its close paralog *HNRNPH1* provide one such example, wherein similar mutations (i.e., missense mutations frequently located in the PY-NLS) cause syndromes with overlapping symptoms (10, 11). Here we investigated the pathological mechanism underlying hnRNPH2-related disorder using in vitro studies, cell lines, and multiple knock-in and KO mouse models. Our results strongly indicate that the mechanism underlying hnRNPH2-related disease is not a simple loss of function but is instead a complex mechanism involving toxic gain of function and/or loss of hnRNPH2 function with inadequate genetic compensation by *HNRNPH1*.

Our in vitro characterization of the consequences of common pathogenic hnRNPH2 mutations revealed, as expected, that mutations in the PY-NLS lead to a partial redistribution of hnRNPH2 protein from the nucleus to the cytoplasm. Notably, this redistribution was modest, with the majority of hnRNPH2 protein remaining in the nucleus. Furthermore, for several pathogenic variants that lie outside the PY-NLS of hnRNPH2, we observed no redistribution of the protein to the cytoplasm.

These findings are complemented by our characterization of KO and knock-in mouse models. Importantly, we found that two independent *Hnrnph2* KO mouse lines were phenotypically normal across a wide variety of measures, with a consistent absence of pathological phenotypes, consistent with ongoing phenotyping of the KOMP KO line reported by the International Mouse Phenotype Consortium. These observations strongly argue that hnRNPH2-related disease cannot be attributed to a simple loss of function. In contrast, *Hnrnph2*^{P209L} and *Hnrnph2*^{R206W} knock-in mice recapitulated the modest redistribution of hnRNPH2 from the nucleus to the cytoplasm while driving a highly penetrant phenotype that reproduced multiple clinical features of human disease, including facial abnormalities, seizure propensity, reduced viability in males, and several behavioral abnormalities, including reductions in motor ability. Indeed, the extensive, robust phenotypes observed in *Hnrnph2*^{P209L}

bioRxiv preprint doi: https://doi.org/10.1101/2022.03.17.484791; this version posted March 19, 2022. The copyright holder for this preprint (which was not certified by peer review) is the author/funder, who has granted bioRxiv a license to display the preprint in perpetuity. It is made available under aCC-BY-NC-ND 4.0 International license.

and *Hnrnph2*^{R206W} mice suggest strong potential for their use in preclinical studies and to reveal novel targets for therapy.

This pattern of phenotypes in physiological models – no apparent phenotypic consequence in KO mice, robust recapitulation of disease features in knock-in mice – suggests two possible mechanisms as drivers of disease. The first possibility is a toxic gain of function, a mechanism with precedents in several common neurological diseases (e.g., ALS caused by mutations in *SOD1*, Parkinson's disease caused by mutations in *SNCA*) in which disease phenotypes are absent in KO animals but are faithfully recapitulated in animals expressing disease mutations. However, our results are also consistent with an alternative disease mechanism in which mutations in *HNRNPH2* directly cause a loss of hnRNPH2 function, but the persistence of significant hnRNPH2 protein in the nucleus results in a failure to induce compensatory *HNRNPH1* expression. Indeed, *HNRNPH1* has an expression pattern that is nearly identical to that of *HNRNPH2* with respect to brain region and cell type, and it encodes a highly similar protein to hnRNPH2. Interestingly, whereas the expression of *HNRNPH1* decreases as development proceeds, the expression of *HNRNPH2* persists, such that cells become progressively more dependent upon hnRNPH2. In this context, our finding that KO of *Hnrnph2* consistently leads to upregulation of *Hnrnph1* suggests that upregulation of *Hnrnph1* is responsible for rescuing KO animals from the consequences of the loss of hnRNPH2 function. In contrast, the introduction of disease mutations in *Hnrnph2* in mice is not accompanied by significant upregulation of *Hnrnph1*. As such, disease-causing mutations in *HNRNPH2* thwart the physiological mechanism that would otherwise compensate for the loss of hnRNPH2 protein function.

Importantly, both of these possible gain-of-function and loss-of-function mechanisms would be predicted to respond positively to therapies designed to deplete expression of mutant proteins (e.g., antisense oligonucleotides). Indeed, genetic compensation between *HNRNPH1* and *HNRNPH2* suggests a therapeutic strategy wherein knockdown of *HNRNPH2* in patients would be predicted to be well tolerated – as KO of *HNRNPH2* is well tolerated in cells and in mice – while also triggering compensatory upregulation of *HNRNPH1*. Further investigation will be needed to determine the mechanisms underlying cross-regulation of *HNRNPH1* and *HNRNPH2*, and how normal functions of hnRNPH2 are disrupted in disease. Of particularly high priority is determining the prospects for therapy aimed at knockdown of mutant *Hnrnph2* to look for upregulation of *Hnrnph1* and potential rescue of the phenotype in mice.

bioRxiv preprint doi: https://doi.org/10.1101/2022.03.17.484791; this version posted March 19, 2022. The copyright holder for this preprint (which was not certified by peer review) is the author/funder, who has granted bioRxiv a license to display the preprint in perpetuity. It is made available under aCC-BY-NC-ND 4.0 International license.

Figure Legends

Figure 1. Pathogenic variants alter the nucleocytoplasmic ratio of hnRNPH2 and enhance its recruitment to RNP granules. (**a**) Schematic representation of hnRNPH2 structure, including mutations identified in patients with a neurodevelopmental disorder. hnRNPH2 contains RNA recognition motifs 1, 2, and 3 (RRM1, RRM2, RRM3), and a nuclear localization signal (PY-NLS). (**b**) Sequence alignment of four human paralogs of the hnRNP F/H family showing high conservation of disease-affected and surrounding residues. Consensus PY-NLS motifs are highlighted in yellow. Amino acids mutated in hnRNPH2 in patients are in red. (**c**) Intracellular localization of FLAG-tagged hnRNPH2 WT, R206W, R206Q, and P209L mutants under basal (left) and stressed (right) conditions in HeLa cells. hnRNPH antibody was used to show endogenous hnRNPH1 and hnRNPH2 localization patterns in untransfected cells. eIF3η was used as a cytoplasmic and stress granule marker. Scale bar, 10 μm. (**d**) Quantification of hnRNPH2 cytosolic signal intensity in HeLa cells as shown in (c). An interleaved scatter plot with individual data points is shown; error bars represent mean ± s.d. For WT, R206W, R206Q, and P209L mutants, n = 24, 19, 21, and 18 cells for basal conditions, n = 24, 19, 22, and 15 cells for stressed conditions, respectively. ****$P < 0.0001$ by one-way ANOVA with Dunnett's multiple comparisons test. (**e**) Summary of intracellular localization of FLAG-tagged hnRNPH2 WT and mutants in HeLa cells. Images are shown in Supplemental Figure 1. Proteins with PY-NLS mutations (red font) showed cytoplasmic accumulation.

Figure 2. Pathogenic variants impair the interaction between hnRNPH2 and its nuclear transport receptor Kapβ2. (**a**) GST pulldown of purified GST-hnRNPH2 peptides with Kapβ2. Proteins bound (left) and unbound (right) to beads are shown. Proteins were visualized by Coomassie Blue staining. (**b**) HEK293T cells were transfected with indicated FLAG-hnRNPH2 constructs, immunoprecipitated for FLAG, and immunoblotted. Kapβ2 binding was reduced in hnRNPH2 variants with PY-NLS mutations. (**c**) Quantification of hnRNPH2 and Kapβ2 interaction from three biological replicates using densitometry from immunoblots as shown in (b). ****$P < 0.0001$ and *$P = 0.0138$ by one-way ANOVA with Dunnett's multiple comparisons test. (**d**) Fluorescent staining of HeLa cells transfected with non-targeting siRNA (siControl) or siRNA targeting *KPNB2*/*TNPO1*. Forty-eight hours post-transfection, cells were treated with 0.5 mM $NaAsO_2$ for 30 min, fixed, and stained with indicated antibodies. G3BP1 was used as a stress granule marker. Scale bar, 10 μm. (**e**) Fluorescent staining of HeLa cells transfected with mCherry or mCherry-M9M. Twenty-four hours post-transfection, cells were fixed and stained

bioRxiv preprint doi: https://doi.org/10.1101/2022.03.17.484791; this version posted March 19, 2022. The copyright holder for this preprint (which was not certified by peer review) is the author/funder, who has granted bioRxiv a license to display the preprint in perpetuity. It is made available under aCC-BY-NC-ND 4.0 International license.

with indicated antibodies. hnRNPA1 was used as a positive control for mCherry-M9M. Scale bar, 10 μm.

Figure 3. Generation, survival, and body weight of *Hnrnph2* mutant and KO mice. (**a**) Schematic of the mouse *Hnrnph2* locus. sgRNA target sequence is shown. Red text indicates protospacer adjacent motif (PAM). (**b**) Nucleotide sequences showing types of editing induced by the sgRNA and single-stranded oligo donor in mouse. Red text indicates edited nucleotide sequences; blue text indicates a premature stop codon introduced by an indel. (**c**) Ratios of genotyped mice organized by sex and breeding strategy. Significant *P* values shown in red (Chi-square test). (**d**) Kaplan-Meier survival curves of male mice up to 8 weeks of age, $*P = 0.0371$ $Hnrnph2^{R206W/Y}$ vs. $Hnrnph2^{X/Y}$; $****P < 0.0001$ $Hnrnph2^{P209L/Y}$ vs. $Hnrnph2^{X/Y}$; $*P = 0.0144$ $Hnrnph2^{KO/Y}$ vs. $Hnrnph2^{X/Y}$ by Mantel-Cox test. (**e**) Mean body weight of male mice over time. $Hnrnph2^{R206W/Y}$ vs. $Hnrnph2^{X/Y}$ $*P < 0.05$ at 8 and 78 weeks, $****P < 0.0001$ at 26, 52, and 104 weeks; $Hnrnph2^{P209L/Y}$ vs. $Hnrnph2^{X/Y}$ $****P < 0.0001$ at 3-6 weeks, $***P < 0.001$ at 7-8 weeks, $**P = 0.0029$ at 26 weeks, $*P = 0.0414$ at 52 weeks, by mixed-effects model (REML) with Sidak's multiple comparisons test. Two *Hnrnph2* KO lines (KO1: C57BL/6NJ-$Hnrnph2^{em1(IMPC)J}$/Mmjax and KO3: TCF02) were used for all analyses and both lines showed the same results. For simplicity, data from our indel-based KO line are included in each graph. Data from the KOMP KO line are summarized in Supplementary Figure 5.

Figure 4. hnRNPH2 mutant mice have craniofacial dysmorphology and an increased incidence of hydrocephalus. (**a**) Representative images of a male $Hnrnph2^{P209L/Y}$ mouse and WT littermate in lateral and dorsal view. (**b**) Key craniofacial parameters measured manually on individual MRI scans. (**c**) Linear measurements in male and female mice. Skull length: $**P = 0.0019$ $Hnrnph2^{R206W/Y}$ vs. $Hnrnph2^{X/Y}$; $****P < 0.0001$ $Hnrnph2^{P209L/Y}$ vs. $Hnrnph2^{X/Y}$; $***P = 0.0006$ $Hnrnph2^{P209L/X}$ vs. $Hnrnph2^{X/X}$. Nose length: $**P = 0.0037$ $Hnrnph2^{R206W/Y}$ vs. $Hnrnph2^{X/Y}$; $****P < 0.0001$ $Hnrnph2^{P209L/Y}$ vs. $Hnrnph2^{X/Y}$; $****P < 0.0001$ $Hnrnph2^{P209L/X}$ vs. $Hnrnph2^{X/X}$. Interorbital distance: $*P = 0.0435$ $Hnrnph2^{R206W/Y}$ vs. $Hnrnph2^{X/Y}$; $*P = 0.0233$ $Hnrnph2^{P209L/Y}$ vs. $Hnrnph2^{X/Y}$, by two-way ANOVA with Sidak's multiple comparisons test . (**d**) Location of 51 landmarks on mouse skull atlas, number of significantly changed linear interlandmark distances, and results of global EDMA analysis. Significant *P* values are shown in red. (**e**) Representative MRI images showing hydrocephalus in a $Hnrnph2^{P209L/Y}$ hemizygous male compared to a WT littermate and incidence of hydrocephalus at 6 ($**P = 0.0035$) and 24 weeks ($***P = 0.0007$, $**P = 0.0041$, $*P = 0.0211$) of age by Fisher's exact test.

bioRxiv preprint doi: https://doi.org/10.1101/2022.03.17.484791; this version posted March 19, 2022. The copyright holder for this preprint (which was not certified by peer review) is the author/funder, who has granted bioRxiv a license to display the preprint in perpetuity. It is made available under aCC-BY-NC-ND 4.0 International license.

Figure 5. hnRNPH2 mutant mice have impaired motor function. (**a**) Total SHIRPA abnormality scores; **P* = 0.0397 *Hnrnph2*$^{P209L/Y}$ vs. *Hnrnph2*$^{X/Y}$ by two-way non-parametric ANOVA with Mann-Whitney U test for groupwise comparisons. (**b**) Latency to fall from rotarod; ***P* = 0.001 *Hnrnph2*$^{R206W/Y}$ vs. *Hnrnph2*$^{X/Y}$; *****P* < 0.0001 *Hnrnph2*$^{P209L/Y}$ vs. *Hnrnph2*$^{X/Y}$; ***P* = 0.0036 *Hnrnph2*$^{P209L/X}$ vs. *Hnrnph2*$^{X/X}$ by two-way ANOVA with Sidak's multiple comparisons test. (**c**) Latency to fall from a wire cage top; ***P* = 0.0017 *Hnrnph2*$^{R206W/Y}$ vs. *Hnrnph2*$^{X/Y}$; ****P* = 0.0005 *Hnrnph2*$^{P209L/Y}$ vs. *Hnrnph2*$^{X/Y}$ by two-way ANOVA with Sidak's multiple comparisons test. (**d**) Quantification of stride length and representative images showing gait of an hnRNPH2 P209L male and WT littermate ; ****P* = 0.0005 *Hnrnph2*$^{P209L/Y}$ vs. *Hnrnph2*$^{X/Y}$; **P* = 0.0265 *Hnrnph2*$^{KO/X}$ vs. *Hnrnph2*$^{X/X}$ by two-way ANOVA with Sidak's multiple comparisons test.

Figure 6. hnRNPH2 mutant mice have increased susceptibility to audiogenic seizures. (**a**) Audiogenic seizure chamber and scoring of seizure behavior. (**b**) Audiogenic seizure severity score; ****P* = 0.0009 *Hnrnph2*$^{P209L/Y}$ vs. *Hnrnph2*$^{X/Y}$; *****P* < 0.0001 *Hnrnph2*$^{R206W/Y}$ vs. *Hnrnph2*$^{X/Y}$; ***P* = 0.0027 *Hnrnph2*$^{P209L/X}$ vs. *Hnrnph2*$^{X/X}$; **P* = 0.026 *Hnrnph2*$^{R206W/X}$ vs. *Hnrnph2*$^{R206W/R206W}$ by two-way non-parametric ANOVA with Mann-Whitney U test for groupwise comparison.

Figure 7. Pathogenic variants alter the nucleocytoplasmic ratio of hnRNPH2 in hnRNPH2 P209L and R206W mice. (**a**) Immunoblot of hnRNPH2 in cortical nuclear fractions. Lamin A/C was used as a loading control; labels 1-3 indicate three biological replicates. (**b**) Quantification of hnRNPH2 normalized to lamin A/C, ***P* = 0.0063 *Hnrnph2*$^{P209L/Y}$ vs. *Hnrnph2*$^{X/Y}$ by two-way ANOVA with Sidak's multiple comparisons test. (**c**) Immunofluorescent staining of hnRNPH2 in mouse brain sections. βIII tubulin and DAPI were used as neuronal cytoplasmic and nuclear markers, respectively. Look-up table (LUT) fire was used to increase the visibility of the hnRNPH2 cytoplasmic signal.

Figure 8. Spatiotemporal expression of *Hnrnph1* and *Hnrnph2* in mouse brain. (**a**) Number of *Hnrnph1* and *Hnrnph2* copies normalized to *Rpp30* in the cortex of *Hnrnph2*^{R206W}, *Hnrnph2*^{P209L}, and *Hnrnph2*^{KO} mice by ddRT-PCR. *HnrnpH1* copies: ***P* = 0.0021 *Hnrnph2*$^{KO/Y}$ vs. *Hnrnph2*$^{X/Y}$; *HnrnpH2* copies: *****P* < 0.0001 *Hnrnph2*$^{KO/Y}$ vs. *Hnrnph2*$^{X/Y}$ by two-way ANOVA with Sidak's multiple comparisons test. (**b**) Number of *Hnrnph1* and *Hnrnph2* copies normalized to *Rpp30* in the cortex of WT C67BL/6J mice across 7 prenatal and postnatal developmental

bioRxiv preprint doi: https://doi.org/10.1101/2022.03.17.484791; this version posted March 19, 2022. The copyright holder for this preprint (which was not certified by peer review) is the author/funder, who has granted bioRxiv a license to display the preprint in perpetuity. It is made available under aCC-BY-NC-ND 4.0 International license.

timepoints by ddRT-PCR; ****P < 0.0001 and **P = 0.006 *Hnrnph1* vs. *Hnrnph2* by two-way ANOVA with Sidak's multiple comparisons test , $^{\#\#\#\#}P$ < 0.0001 *Hnrnph1* E16.5 vs. P0, P0 vs. P7, $^{\#\#}P$ = 0.0049 *Hnrnph1* P7 vs. P14 by two-way ANOVA with Tukey's multiple comparisons test. (**c**) H-scores for *Hnrnph1* and *Hnrnph2* probes in the brain of WT C67BL/6J mice across 7 prenatal and postnatal developmental timepoints by Halo analysis of BaseScope ISH; ****P < 0.0001 *Hnrnph1* vs. *Hnrnph2* at E12.5 – P7 and **P = 0.0018 *Hnrnph1* vs. *Hnrnph2* at P14 by two-way ANOVA with Sidak's multiple comparisons test, $^{\#\#\#\#}P$ < 0.0001 *Hnrnph1* E12.5 vs. E14.5, $^{\#}P$ = 0.046 *Hnrnph1* P14 vs. P56 by two-way ANOVA with Tukey's multiple comparisons test. (**d**) Regional expression of *Hnrnph1* and *Hnrnph2* across the adult (P56) mouse brain by BaseScope ISH. White arrowheads show the location of the corpus callosum, asterisks indicate the location of fiber tracts. Ob, olfactory bulb; CC, corpus callosum; IC, cerebral cortex/isocortex; H/DG, hippocampus/dentate gyrus; St, bed of nuclei of the stria terminalis; P, pons; M, medulla; Th, thalamus; Mb, rostral collicular midbrain; Cb, cerebellum; Cbc, cerebellar cortex; wmft, white matter fiber tracts. (**e**) Expression of *Hnrnph1* and *Hnrnph2* in the major classes of brain cells at P7 by RNA-seq (36, 37). FPKM, fragments per kilobase of transcript per million mapped reads. (**f**) Top 5 expression cell clusters for *Hnrnph1* and *Hnrnph2* in the adult mouse brain by single-cell RNA-seq (38).

bioRxiv preprint doi: https://doi.org/10.1101/2022.03.17.484791; this version posted March 19, 2022. The copyright holder for this preprint (which was not certified by peer review) is the author/funder, who has granted bioRxiv a license to display the preprint in perpetuity. It is made available under aCC-BY-NC-ND 4.0 International license.

Supplementary Figure Legends

Supplementary Figure 1. Pathogenic variants alter the nucleocytoplasmic ratio of hnRNPH2 and enhance its recruitment to RNA granules. Intracellular localization of indicated FLAG-tagged hnRNPH2 proteins under basal (left) and stressed (right) conditions in HeLa cells. eIF3η was used as a cytoplasmic and stress granule marker. Scale bar, 10 μm.

Supplementary Figure 2. Frameshift variants impair the interaction between hnRNPH2 and its nuclear transport receptor Kapβ2. (**a**) hnRNPH2 amino acid sequence used for GST pulldown experiments. Amino acid residues mutated in patients are in red. (**b-e**) Peptides spanning amino acids 184-210, 179-215, 174-220, or 169-225 were fused to the C terminus of GST. Gels show Coomassie Blue staining following GST pulldown of purified GST-hnRNPH2 peptides with Kapβ2. (**f**) Immunoblot showing knockdown of Kapβ2 by si*KPNB2*. Three independently prepared samples were loaded on the gel. Graph shows relative Kapβ2 levels normalized to actin; error bars represent mean ± s.d. ****$P < 0.0001$ by student's t-test.

Supplementary Figure 3. Sequence alignment of human and mouse hnRNPH2 proteins. Human hnRNPH2 and mouse hnRNPH2 are highly conserved. Both proteins are composed of 449 amino acids, of which only 4 amino acids differ. The PY-NLS motif (yellow highlight) within the PY-NLS (gray highlight) is absolutely conserved between the two species.

Supplementary Figure 4. Generation and validation of *Hnrnph2* mutant and KO mouse lines. (**a**) Off-target analysis of knock-in mice generated. Lines CFD01, TCF03, and TCF02 were selected for *Hnrnph2*^{R206W}, *Hnrnph2*^{P209L}, and *Hnrnph2*^{KO} genotypes, respectively, for further experiments. (**b**) Western blot of hnRNPH2 expression in cortex of WT, commercially available *Hnrnph2* KO line (KO1, C57BL/6NJ-*Hnrnph2*$^{em1(IMPC)J}$/Mmjax), and two KO lines we generated (KO2 (TCF42) and KO3 (TCF02)). KO3 (line TCF02) was chosen as the *Hnrnph2* KO line for further experiments. (**c**) Expression of *Hnrnph2* transcript by ddRT-PCR in the cortex of *Hnrnph2* KO (KO3 (TCF02)) mice. Normalization to *Gapdh* and *Rpp30* are shown. *$P = 0.0121$ WT males vs. hemizygous *Hnrnph2* KO males with normalization to *Gapdh*, $^{###}P = 0.0001$ WT males vs. hemizygous *Hnrnph2* KO males with normalization to *Rpp30*, $^{\#}P = 0.0153$ WT females vs. homozygous *Hnrnph2* KO females with normalization to *Rpp30,* by one-way ANOVA with Sidak's multiple comparisons test. (**d**) Immunofluorescent staining of hnRNPH2 in brain sections of WT, a commercially available *Hnrnph2* KO line (KO1), and a newly generated *Hnrnph2* KO line (KO3). NeuN and βIII tubulin were used as neuronal nuclear and cytoplasmic

bioRxiv preprint doi: https://doi.org/10.1101/2022.03.17.484791; this version posted March 19, 2022. The copyright holder for this preprint (which was not certified by peer review) is the author/funder, who has granted bioRxiv a license to display the preprint in perpetuity. It is made available under aCC-BY-NC-ND 4.0 International license.

markers, respectively.

Supplementary Figure 5. Summary of data from *Hnrnph2*$^{em1(IMPC)J}$/Mmjax KO mice. (**a**) Ratios of genotyped mice organized by sex and breeding strategy. (**b**) Kaplan-Meier survival curves of male and female mice up to 8 weeks of age. (**c**) Kaplan-Meier survival curves of male and female mice up to 2 years of age. (**d**) Mean body weight of male and female mice over time. (**e**) Linear measurements of key craniofacial parameters in hemizygous male and heterozygous female mice. (**f**) Number of significantly changed linear inter-landmark distances (top) and results of global EDMA analysis (bottom). (**g**) P values for regional EDMA analysis for hemizygous males and heterozygous females. (**h**) Incidence of hydrocephalus at 6 and 24 weeks of age. (**i**) Number of mice found dead or flagged for domed heads with pathologically confirmed hydrocephalus. (**j-m**) Characterization of hemizygous male and heterozygous female mice showing (j) total SHIRPA abnormality scores, (k) latency to fall from rotarod, (l) latency to fall from a wire cage top, and (m) quantification of stride length. (**n-o**) Subdomain SHIRPA scores for hemizygous male and heterozygous female mice are shown for (n) motor function and (o) autonomic function. (**p-s**) Characterization of hemizygous male and heterozygous female mice showing (p) latency to cross a balance beam, (q) grip strength, (r) optomotor response test of visual acuity, and (s) hot plate test of pain response. (**t**) Audiogenic seizure severity scores. (**u**) Number of copies of *Hnrnph1*, *Hnrnph2*, *Hnrnpf*, and *Hnrnph3* normalized to *Rpp30* in the cortex of *Hnrnph2*$^{em1(IMPC)J}$/Mmjax hemizygous male and heterozygous female KO mice by ddRT-PCR. In all analyses, WT mice are littermate controls.

Supplementary Figure 6. Survival and body weight of *Hnrnph2* mice. (**a-b**) Kaplan-Meier survival curves of female heterozygous (a) and homozygous (b) mice up to 8 weeks of age. (**c**) Kaplan-Meier survival curves of male and female mice up to 2 years of age. (**d**) Mean body weight of female mice over time; *Hnrnph2*$^{R206W/X}$ vs. *Hnrnph2*$^{X/X}$ $^{**}P < 0.01$ at 26, 52, and 78 weeks, $^{*}P = 0.045$ at 104 weeks by mixed-effects model (REML) with Sidak's multiple comparisons test.

Supplementary Figure 7. Craniofacial dysmorphology and hydrocephalus in *Hnrnph2* mice. (**a**) Key craniofacial parameters measured manually on individual MRI scans. Lower jaw length: $^{****}P < 0.0001$ *Hnrnph2*$^{P209L/Y}$ vs. *Hnrnph2*$^{X/Y}$; upper jaw: $^{**}P = 0.0014$ *Hnrnph2*$^{R206W/Y}$ vs. *Hnrnph2*$^{X/Y}$; $^{****}P < 0.0001$ *Hnrnph2*$^{P209L/Y}$ vs. *Hnrnph2*$^{X/Y}$; $^{*}P = 0.0139$ *Hnrnph2*$^{P209L/X}$ vs. *Hnrnph2*$^{X/X}$ by two-way ANOVA with Sidak's multiple comparisons test. (**b**) Figure depicting the

bioRxiv preprint doi: https://doi.org/10.1101/2022.03.17.484791; this version posted March 19, 2022. The copyright holder for this preprint (which was not certified by peer review) is the author/funder, who has granted bioRxiv a license to display the preprint in perpetuity. It is made available under aCC-BY-NC-ND 4.0 International license.

subset of anatomically relevant landmarks used in the regional EDMA analysis and P values of the regional EDMA analysis. (**c**) Number of mice found dead or flagged for domed heads with pathologically confirmed hydrocephalus. (**d**) H&E staining showing patent aqueducts in hnRNPH2 P209L and hnRNPH2 R206W mice with hydrocephalus. (**e**) Representative MRI images showing hydrocephalus in a *Hnrnph2*$^{R206W/X}$ heterozygous female compared with a WT littermate.

Supplementary Figure 8. H&E staining, Luxol fast blue-cresyl violet (LFB-CV) staining, and immunohistochemistry in hnRNPH2 P209L mouse brains. H&E and LFB-CV staining showing no gross abnormalities in the brains of hnRNPH2 P209L males compared to WT littermates. Immunohistochemistry with markers against oligodendrocytes (OLIG2), astrocytes (GFAP), and microglia (IBA1) was also normal. Representative images of the primary motor and somatosensory cortex for each stain and marker are shown. Quantification of LFB-CV staining, and OLIG2, GFAP, and IBA1 immunoreactivity in the whole brain are shown.

Supplementary Figure 9. Cortical neuronal count and distribution in *Hnrnph2* mice. (**a**) Immunohistochemistry with NeuN in a WT mouse brain with manual annotation of visual, somatosensory, and somatomotor cortex. (**b**) Quantification of neurons in somatosensory, somatomotor, and visual cortex. The number of NeuN-positive cells per mm^2 is shown. (**c**) Immunofluorescence with cortical layer-specific markers SATB2 (layer II-IV), CTIP2 (layer V), and FOXP2 (layer VI) performed in WT, hnRNPH2 R206W, hnRNPH2 P209L, and *Hnrnph2* KO male mice. Regions of interest were positioned over the visual, somatomotor, and somatosensory cortex and subdivided into 8 equal bins. (**d-f**) The number of SATB2-, CTIP2-, and FOXP2-positive cells were counted and expressed as a percentage of the total number of DAPI-positive cells within each bin in the visual (d), somatosensory (e), and somatomotor cortex (f) as defined in panel (c).

Supplementary Figure 10. *Hnrnph2* mutant mice have impaired motor function. (**a-b**) Subdomain SHIRPA scores are shown. Motor function (a): $^{**}P < 0.01$ *Hnrnph2*$^{R206W/Y}$ vs. *Hnrnph2*$^{X/Y}$; $^{**}P < 0.001$ *Hnrnph2*$^{P209L/Y}$ vs. *Hnrnph2*$^{X/Y}$; $^{**}P = 0.001$ *Hnrnph2*$^{P209L/X}$ vs. *Hnrnph2*$^{X/X}$. Autonomic function (b): $^{***}P = 0.0003$ *Hnrnph2*$^{KO/Y}$ vs. *Hnrnph2*$^{X/Y}$; $^{*}P = 0.017$ *Hnrnph2*$^{P209L/X}$ vs. *Hnrnph2*$^{X/X}$ by two-way non-parametric ANOVA with Mann-Whitney U test for group wise comparisons. (**c**) Latency to cross balance beam, $^{****}P < 0.0001$ *Hnrnph2*$^{R206W/Y}$ vs. *Hnrnph2*$^{X/Y}$; $^{*}P = 0.0264$ *Hnrnph2*$^{P209L/Y}$ vs. *Hnrnph2*$^{X/Y}$. (**d**) Grip strength, $^{**}P = 0.0065$

bioRxiv preprint doi: https://doi.org/10.1101/2022.03.17.484791; this version posted March 19, 2022. The copyright holder for this preprint (which was not certified by peer review) is the author/funder, who has granted bioRxiv a license to display the preprint in perpetuity. It is made available under aCC-BY-NC-ND 4.0 International license.

Hnrnph2$^{P209L/Y}$ vs. *Hnrnph2*$^{X/Y}$ by two-way ANOVA with Sidak's multiple comparisons test.

Supplementary Figure 11. *Hnrnph2* mutant mice have normal sensory function. (**a**) Optomotor response test of visual acuity. (**b**) Hot plate test of pain response. (**c**) Scent habituation test of olfaction.

Supplementary Figure 11. Spatiotemporal expression of *HNRNPH1* and *HNRNPH2* in human brain and cortical organoids. (**a**) Immunoblot and quantification of hnRNPH1 expression in whole brain RIPA-soluble fractions. GAPDH was used as a loading control; **P* = 0.0454 WT vs. *Hnrnph2* KO by t-test. (**b**) Number of *Hnrnpf* and *Hnrnph3* copies normalized to *Rpp30* in the cortex of *Hnrnph2*^{R206W}, *Hnrnph2*^{P209L}, and *Hnrnph2*^{KO} mice by ddRT-PCR. (**c**) Trajectory plot showing the expression of *HNRNPH1* and *HNRNPH2* in 6 major brain regions across 15 developmental time points by Affymetrix GeneChip Human Exon 1.0 ST Arrays. Period 1-7, fetal development; solid line, birth; period 8-9, infancy; period 10-11, childhood; period 12, adolescence; period 13-15, adulthood. Neocortex (NCX), hippocampus (HIP), amygdala region (AMY), striatum (STR), mediodorsal nucleus of the thalamus (MD), and cerebellar cortex (CBC) are shown. Reprinted from the Human Brain Transcriptome dataset (33, 40, 41). (**d**) Violin plots showing the expression of *HNRNPH1* and *HNRNPH2* in 13 brain regions by RNA-seq. Data used for the analyses described here were obtained from the Genotype-Tissue Expression (GTEx) Portal, dbGaP accession number: phs000424.v8.p2. TPM, transcripts per million. (**e**) Trajectory plot showing the expression of *HNRNPH1* and *HNRNPH2* in human cortical organoids across differentiation day and mapped BrainSpan stages by RNA-seq. Stage 3-7, fetal development; stage 8, birth to 6 months; stage 9, 6 months to 19 months. Transition from prenatal to postnatal stages are indicated with a horizontal grey area/line. Reprinted from the Gene Expression in Cortical Organoids dataset (35).

bioRxiv preprint doi: https://doi.org/10.1101/2022.03.17.484791; this version posted March 19, 2022. The copyright holder for this preprint (which was not certified by peer review) is the author/funder, who has granted bioRxiv a license to display the preprint in perpetuity. It is made available under aCC-BY-NC-ND 4.0 International license.

Acknowledgments

We thank members of the St. Jude Center for In Vivo Imaging and Therapeutics, the Department of Diagnostic Imaging, and the Developmental Neurobiology behavior core for assistance with MRI, uCT, and sensory function testing, including Jieun Kim, Young Sang Ryo, Kaitlin Lord, Matthew Scoggins, Silu Zhang, Bogdan Mitrea, Donnie Eddins, and Lauren Beloate. We thank Natalia Nedelsky for editorial assistance. This work was supported by the Howard Hughes Medical Institute and R35NS097974 grants to J.P.T.

Author contributions

A.K., X.Y., K.O., F.Y., and A.G. designed and performed laboratory experiments. A.K., T.P., H.T., Y.M.C., J.P.T., and H.J.K. analyzed data. A.K., J.P.T., and H.J.K. drafted and revised the manuscript. J.P.T. and H.J.K. supervised the overall study.

Disclosures

JPT is a consultant for Nido Biosciences and Faze Medicines.

Methods

Cell Culture and Transfection

HEK293T and HeLa cells were grown in Dulbecco's modified Eagle's medium (DMEM) supplemented with 10% fetal bovine serum (FBS), 1% penicillin/streptomycin, and 1% L-glutamate. Cells were counted using ADAM-CellT (NanoEntek Inc., Seoul, Korea), plated and transfected using Lipofectamine 3000 (ThermoFisher; L3000008) for transient overexpression or RNAiMAX (ThermoFisher; 13778075) for siRNA knockdown according to the manufacturer's instructions.

Immunofluorescence and Microscopy in Human Cell Lines

HeLa cells were seeded on 8-well glass slides (Millipore). Twenty-four hours post transfection for overexpression or 72 hours post transfection for siRNA knockdown, cells were stressed with 500 μM sodium arsenite (Sigma-Aldrich) for times as indicated in text and legends. Cells were then fixed with 4% paraformaldehyde (Electron Microscopy Sciences), permeabilized with 0.5% Triton X-100, and blocked in 5% bovine serum albumin (BSA). Primary antibodies used were mouse monoclonal anti-FLAG (M2, F1804; Sigma), goat polyclonal anti-eIF3η (sc-16377; Santa

bioRxiv preprint doi: https://doi.org/10.1101/2022.03.17.484791; this version posted March 19, 2022. The copyright holder for this preprint (which was not certified by peer review) is the author/funder, who has granted bioRxiv a license to display the preprint in perpetuity. It is made available under aCC-BY-NC-ND 4.0 International license.

Cruz Biotechnology), rabbit monoclonal anti-hnRNPH2 (ab179439; Abcam), mouse monoclonal anti-G3BP (BD Biosciences; 611126), and mouse monoclonal anti-hnRNPA1 (Millipore; 05-1521). For visualization, the appropriate host-specific Alexa Fluor 488, 555, or 647 (Invitrogen) secondary antibody was used. Slides were mounted using Prolong Gold Antifade Reagent with DAPI (Life Technologies). Images were captured using a Leica TCS SP8 STED 3X confocal microscope (Leica Biosystems) with a 63x objective. Fluorescent images were subjected to automated compartmentalization analysis using CellProfiler software (Broad Institute). Cells were segmented using DAPI and eIF3η channels to identify the nucleus and cytoplasm. Integrated intensity of nucleus, cytoplasm, and cells were measured. Percent cytoplasmic signal was calculated with the integrated cytoplasmic signal over the integrated cell signal.

Immunoprecipitation and Western Blot Analysis

Cell lysates were prepared by lysing cells in buffer containing 20 mM phosphate buffer pH 7.5, 150 mM NaCl, 0.2% Triton X-100, and 10% glycerol with complete protease inhibitor cocktail (Clontech Laboratories). Cells were incubated on ice for 20 min before centrifugation at 14,000 rpm at 4°C. The resulting supernatant was pre-treated with EZView Red Protein A agarose beads (P6486; Sigma) for 45 min to reduce the likelihood of nonspecific binding to the agarose, and the beads were removed. EZView Red Anti-FLAG M2 agarose beads (F2426; Sigma) were then added to the pre-treated lysates and incubated at 4°C for 2 h. The agarose beads were washed three times with buffer above to remove any remaining nonspecific binding. Samples were eluted with FLAG peptide (F3290; Sigma) at a final concentration of 100 µg/ml for 30 min at vortex setting 5 (Scientific Industries) at 4°C. Samples were boiled in 1x LDS sample buffer (ThermoFisher). Samples were resolved by electrophoresis on a NuPAGE Novex 4-12% Bis-Tris Gel (Invitrogen). Gels were transferred to nitrocellulose using an iBlot 2 gel transfer device (ThermoFisher) and blocked in 5% BSA. Primary antibodies used were rabbit polyclonal anti-FLAG (F7425; Sigma) and mouse monoclonal anti-Kapβ2 (ab10303; Abcam). Blots were subsequently incubated with IRDye fluorescence antibodies (LI-COR) and protein bands were visualized using the Odyssey Fc system (LI-COR) and Image Studio (LI-COR). Bands were quantified by densitometry in ImageJ (NIH).

Pull-down Assays for Kapβ2 Binding to Immobilized GST-hnRNPH2 Peptides

E. coli (BL21) transformed with pGEX-4TT3 plasmids expressing GST-hnRNPH2 proteins were grown in 35 ml LB with 100 µg/ml ampicillin to OD_{600} 0.6. Protein expression was then induced with 0.5 mM isopropyl-β-d-1-thiogalactoside (IPTG) for 5 h at 37°C. Cells were harvested by

bioRxiv preprint doi: https://doi.org/10.1101/2022.03.17.484791; this version posted March 19, 2022. The copyright holder for this preprint (which was not certified by peer review) is the author/funder, who has granted bioRxiv a license to display the preprint in perpetuity. It is made available under aCC-BY-NC-ND 4.0 International license.

centrifugation, resuspended in lysis buffer (50 mM Tris pH 7.4, 150 mM NaCl, 1 mM EDTA, 2 mM DTT, 15% glycerol, and protease inhibitors), lysed by sonication, the lysate centrifuged, and supernatant containing GST-hnRNPH2 proteins added to Glutathione Sepharose 4B (GSH; GE Healthcare) beads. The beads with immobilized GST-hnRNPH2 proteins were washed with lysis buffer. 50 µl beads containing ~60 µg immobilized GST-hnRNPH2 proteins were incubated with 8 µM Kapβ2 in 100 µl total volume for 30 min at 4°C and then washed three times with 1 ml lysis buffer. Proteins bound on the beads were eluted by boiling in SDS sample buffer and visualized by Coomassie staining of SDS-PAGE gels.

Generation of *Hnrnph2* Mutant and Knockout Mice

gRNA was in vitro transcribed using MEGA shortscript T7 kit (Life Tech Corp AM1354), and the template PCR amplified using the following primers:

Forward: 5′ -
CCTTAATACGACTCACTATAGGGCTCATGACTATGCAGCGCCGTTTTAGAGCTAGAAATAG
C-3′

Reverse: 5′-
AAAAGCACCGACTCGGTGCCACTTTTTCAAGTTGATAACGGACTAGCCTTATTTTAACTTGC
TATTTCT AGCTCTAAAAC-3′

The resulting PCR products contained the T7 promoter, gRNA sequence, and tracrRNA (5′-
CCTTAATACGACTCACTATAGGGCTCATGACTATGCAGCGCCGTTTTAGAGCTAGAAATAG
CAAGTTAAAATAAGGCTAGTCCGTTATCAACTTGAAAAAGTGGCACCGAGTCGGTGCTTTT-
3′). Synthetic single-strand DNA was used as mutation donor. Donor DNA sequences are shown below.

P209L: 5′-
ACAAGGAAAGAATAGGGCATAGGTACATCGAAATCTTCAAGAGTAGCCGAGCTGAAGTCC
GAACCCA
CTATGATCCACCTAGAAAGCTCATGACTATGCAGCGCCCGGGTCTTTACGATAGGCCAGG
GGCTGGAAGAGGGTATAATAGCATTGGCAGAGGAGCCGGGTTTGAAAGAATGAGGCGGG
GTGCCTATGGTGGA-3′

R206W: 5′-
AACACAAGGAAAGAATAGGGCATAGGTACATCGAAATCTTCAAGAGTAGCCGAGCTGAAGT
CCGAA
CCCACTATGATCCACCTAGAAAGCTCATGACTATGCAGTGGCCGGGTCCTTACGATAGGC
CAGGGGCTGGAAGAGGGTATAATAGCATTGGCAGAGGAGCCGGGTTTGAAAGAATGAGG

bioRxiv preprint doi: https://doi.org/10.1101/2022.03.17.484791; this version posted March 19, 2022. The copyright holder for this preprint (which was not certified by peer review) is the author/funder, who has granted bioRxiv a license to display the preprint in perpetuity. It is made available under aCC-BY-NC-ND 4.0 International license.

CGGGGTGCCTATGGT-3′

The gRNAs, Cas9 mRNA, and ssDNA were co-microinjected into C57BL/6J zygotes at 25, 25, and 10 ng/μl respectively. Seven mice with P209L and 11 mice with R206W mutations were identified by PCR (5′- GACACTGCCAGTGGACTTTC - 3′ and 5′- TGCTCTGGAAACTGGACCCA - 3′) followed by sequencing (5′- TGCTCTGGAAACTGGACCCA - 3′). These potential founders were crossed with WT C57BL/6J mice to confirm transmission of the mutation. Resulting progeny carrying the mutations were tested for possible off-target effects as predicted by the Wellcome Sanger Institute Genome Editing Off-Target by Sequence tool (42). Of the 61 predicted off-target sites (1: 0, 2: 0, 3: 9, 4: 52), all nine 3-nucleotide mismatch sites were tested by high-resolution melt analysis. All but one of the lines tested showed no off-target effects at these sites (**Supplementary Fig. 4**). One line gave variant calls on all 9 sites, which was attributed to low DNA concentration of the sample. Nevertheless, this line was discarded. One line of each mutation (P209L, R206W, and KO) was chosen for phenotyping and heterozygous mutant or KO females bred to C57BL/6J males to maintain the genetic background. Subsequent generations were genotyped by Transnetyx automated real-time PCR (Transnetyx).

Breeding of Experimental Cohorts

For most experiments, heterozygous mutant females were bred to WT males to generate heterozygous mutant or KO females (*Hnrnph2*$^{R206W/X}$, *Hnrnph2*$^{P209L/X}$, *Hnrnph2*$^{KO/X}$), hemizygous mutant or KO males (*Hnrnph2*$^{R206W/Y}$, *Hnrnph2*$^{P209L/Y}$, *Hnrnph2*$^{KO/Y}$), WT females (*Hnrnph2*$^{X/X}$), and WT males (*Hnrnph2*$^{X/Y}$). In addition, for some experiments heterozygous mutant females were bred to hemizygous mutant males to generate homozygous mutant or KO females (*Hnrnph2*$^{R206W/R206W}$, *Hnrnph2*$^{KO/KO}$), heterozygous mutant or KO females (*Hnrnph2*$^{R206W/X}$, *Hnrnph2*$^{KO/X}$), hemizygous mutant or KO males (*Hnrnph2*$^{R206W/Y}$, *Hnrnph2*$^{KO/Y}$), and WT males *Hnrnph2*$^{X/Y}$. Note that this cross could not be performed in the *Hnrnph2*^{P209L} line, as very few *Hnrnph2*$^{P209L/Y}$ males survived until sexual maturity (6-8 weeks). All experiments were performed on generation F3 or later. Animals were group housed under standard conditions and all studies were approved by the St. Jude Children's Research Hospital institutional review committee on animal safety.

Mendelian Inheritance and Survival up to 8 Weeks

All pups born and genotyped (samples collected from live pups at P2-P7 and from pups found dead before P2-P7 sample collection) were included in calculation of genotype ratios. All pups

bioRxiv preprint doi: https://doi.org/10.1101/2022.03.17.484791; this version posted March 19, 2022. The copyright holder for this preprint (which was not certified by peer review) is the author/funder, who has granted bioRxiv a license to display the preprint in perpetuity. It is made available under aCC-BY-NC-ND 4.0 International license.

born and genotyped were also included in survival analyses, except for mice used in cohort 2 (audiogenic seizure cohort) and cohort 3 (μCT and imaging cohort).

Behavioral Phenotyping and Long-Term Survival

Experimental cohort 1, consisting of male hemizygous mutants or KOs, female heterozygous mutants or KOs, and WT littermate controls, were first subjected to an observational test battery at 8 weeks old. This was followed by more specific and sensitive tests of motor and sensory function at 8-9 weeks and 10-12 weeks, respectively. These mice were also weighed weekly from 3 to 8 weeks, then again at 6 months and every 6 months thereafter and followed for survival.

A slightly modified protocol of the EMPReSS (European Mouse Phenotyping Resource for Standardized Screens) version of SHIRPA (SmithKline Beecham, Harwell, Imperial College, Royal London Hospital, Phenotype Assessment) level 1 observational test battery was used (27). Briefly, mice were observed undisturbed in a clear viewing jar for activity, tremor, palpebral closure, coat appearance, skin color, whisker appearance, lacrimation, defecation, and urination. Mice were then moved to an arena and the following parameters scored: transfer arousal, locomotor activity, gait, pelvic elevation, tail elevation, startle response, touch escape and righting reflex. Thereafter, mice were held by the tail and scored for positional passivity, trunk curl, limb clasping, and visual placing. After placement on a wire mesh grid, mice were then assessed for corneal reflex, pinna reflex, whisker orienting reflex, toe pinch response, and negative geotaxis. Lastly, contact righting response when place in a tube and rolled upside down was tested, and any evidence of biting and excessive vocalization noted. The data were quantified using a binary scoring system as previously described (43). A normal behavior received a score of 0 and an abnormal behavior received a score of 1, enabling a global abnormality score to be determined for each mouse, with a higher score corresponding to a greater degree of abnormality. In addition, scores were also generated for specific functions including motor, sensory, neuropsychiatric, and autonomic function (28).

Rotarod analysis was performed on an accelerating rotarod apparatus (IITC Life Science) using a 2-day protocol. Mice were trained on the first day with one session set at 4 rpm for 5 min. The following day, rotation speed was set to accelerate from 4 to 40 rpm at 0.1 rpm/s, mice were placed on the apparatus, and the latency to fall was recorded for four separate trials per mouse. Mice were given a 15-min rest period between each trial. Grip strength was measured using a grip strength meter (Bioseb) as grams of force for all 4 paws for each mouse in six repeated measurements. The beam walking test was performed using a 2-day, multi-

bioRxiv preprint doi: https://doi.org/10.1101/2022.03.17.484791; this version posted March 19, 2022. The copyright holder for this preprint (which was not certified by peer review) is the author/funder, who has granted bioRxiv a license to display the preprint in perpetuity. It is made available under aCC-BY-NC-ND 4.0 International license.

beam protocol (44). Briefly, on day 1 mice were trained to walk across an elevated 12-mm square beam to reach an enclosed goal box. On day 2, mice received one trial each on a 12-mm square beam, a 6-mm square beam, and a 12-mm round beam, and latency to cross, number of hind paw slips, and number of falls recorded. A custom neurological scoring system was also used, where a score of 0 was given if the mouse was unable to traverse the beam in 60 s, 1 if a mouse traversed the entire beam by dragging itself with its front paws (hind paws remain in contact with the side of the beam at all times), 2 if a mouse was able to traverse the beam with some hind paw stepping on top of the beam before starting to drag itself with its front paws, 3 if a mouse was able to traverse the entire beam with hind paw stepping, but placed its hind paws on the side of the beam at least once (no dragging with front paws), and 4 if a mouse was able to traverse the entire beam with hind paw stepping and never placing its hind paws on the side of the beam. In the wire hang test, mice were placed onto a wire cage top, which was then inverted and elevated above a clean cage, and latency to fall (up to 120 s) recorded. For gait analysis, the front and hind paws of each animal were dipped in red and blue paint (water-soluble and non-toxic), respectively. The animal was then placed in a 70-cm long tunnel lined on the bottom with Whatman filter paper, the entrance sealed, and animal allowed to walk through one time. Footprints were scanned and analyzed with Image J for stride length, fore- and hind base width, and overlap (45).

Experimental cohort 2, consisting of male hemizygous mutants or KOs, female heterozygous mutants or KOs, female homozygous mutants or KOs, and WT littermate controls, were tested for audiogenic seizure susceptibility in a clear acrylic box (30 x 30 x 30 cm), with a 6” red fire bell mounted to the underside of a removable lid, and connected to a standard GraLab timer. The bell consistently produced 120-125 dB sound as measured from inside the closed box using a digital sound level meter. At P21, mice were removed from their home cage one by one just before testing, put into a clean holding cage, and moved to the testing room. Mice were then transferred to the audiogenic seizure chamber and allowed to explore the box for 15 s before the bell was turned on for 60 s. The intensity of the response (seizure severity score) was categorized as 0 for no response or slight startle, 1 for wild running, 2 for clonic seizures, 3 for tonic seizures, and 4 for respiratory arrest (46).

In Vivo MRI and µCT

Experimental cohort 3, consisting of male hemizygous mutants or KOs, female heterozygous mutants or KOs, and WT littermate controls, were imaged at the Center for In Vivo Imaging and Therapeutics at St. Jude Children’s Research Hospital using micro-computed tomography (µCT)

bioRxiv preprint doi: https://doi.org/10.1101/2022.03.17.484791; this version posted March 19, 2022. The copyright holder for this preprint (which was not certified by peer review) is the author/funder, who has granted bioRxiv a license to display the preprint in perpetuity. It is made available under aCC-BY-NC-ND 4.0 International license.

and magnetic resonance imaging (MRI) at 6 and 24 weeks of age. The μCT was performed on a Siemens Inveon PET/CT system (Siemens) at 88-μm resolution, and the MRI was performed on a Bruker Clinscan 7T MRI system (Bruker Biospin MRI GmbH). MRI was acquired with a mouse brain surface receive coil positioned over the mouse head and placed inside a 72-mm transmit/receive coil. After the localizer, a T2-weighted turbo spin echo sequence with variable flip-angle echo trains was performed in the coronal orientation (TR/TE = 2500/114 ms, matrix size = 192 × 192 x 104, resolution = 0.12 x 0.12 x 0.12 mm, number of averages = 4). Prior to scanning, mice were anesthetized in a chamber (3% isoflurane in oxygen delivered at 1 L/min) and maintained using nose-cone delivery (1-2% isoflurane in oxygen delivered at 1 L/min). Animals were provided thermal support using an inbuilt electronic heating pad (μCT) or a heated bed with warm water circulation (MRI) and a physiological monitoring system to monitor breath rate. After imaging, animals were allowed to recover on a heating pad.

Morphometric analysis was performed on the μCT images to identify group differences in skull shape. Linear measurements of 11 key craniofacial parameters (20) were performed manually on μCT slices using Inveon Research Workplace software (IRW 4.2, Siemens). This was followed by automated imaged-based shape analysis using a population-level atlas of the *Mus musculus* craniofacial skeleton (21). Briefly, the head was extracted from the whole-body μCT images using an iterative search and best-match algorithm. The μCT atlas (https://github.com/muratmaga/mouse_CT_atlas) was then aligned to native space images using a first pass affine transform, followed by a non-linear warping. The calculated transform was then applied to a set of 51 previously identified landmarks and the coordinates for the landmarks in native space were extracted. Processing steps were performed using the ANTS software package (https://github.com/ANTsX/ANTsPy). All alignment results were visually inspected by at least 2 raters. The Euclidean distance between each point was calculated and used for subsequent analysis. First, we performed pairwise comparisons of linear distances between all 51 landmarks. Next, we performed Euclidean distance matrix analysis (EDMA), a geometric morphometric approach enabling the quantification and comparison of shape in three dimensions (22). For global EDMA analysis all 51 landmarks were included, whereas the regional EDMA analysis was performed on a subset of landmarks that summarize regions with specific embryonic tissue origins, further divided into anatomically relevant subsets including palate, midface, and nasal regions (24). To account for overall difference in size, both the global and regional EDMA analyses were scaled to centroid size (calculated as the square root of the sum of squared distances of all landmarks from their centroid), which is a common proxy for overall size in geometric morphometric analyses (23).

bioRxiv preprint doi: https://doi.org/10.1101/2022.03.17.484791; this version posted March 19, 2022. The copyright holder for this preprint (which was not certified by peer review) is the author/funder, who has granted bioRxiv a license to display the preprint in perpetuity. It is made available under aCC-BY-NC-ND 4.0 International license.

Brain parcellation and volumetrics were performed to investigate group differences in regional brain volumes. We used the DSURQE atlas (26), which contains 336 cortical, white matter, subcortical, and CSF defined regions. The DSURQE anatomical image was first down-sampled to a resolution of 120 micron isotropic to satisfy the Nyquist criteria of our image resolution and reduce computational time for fitting. The acquired T2 images were preprocessed, including skull-stripping and intensity normalization. The images were then aligned to the atlas by a first-pass affine registration, followed by a non-linear warping. The inverse warping was applied to the labeled atlas to bring all labeled areas into native space. All image processing steps were performed using the AFNI software package (https://afni.nimh.nih.gov/). The volume (number of voxels times native resolution) of each labeled area from the atlas was extracted for subsequent analysis. The results of the inverse warping were quality checked by visual inspection by at least 2 raters. Cases with poor alignment (17 out of a total of 140) were removed from the final volumetric analysis.

Mouse Histology and Immunofluorescence

For confirmation of hydrocephalus, mice were anesthetized by isoflurane inhalation and transcardially perfused with 10% neutral buffered formalin (NBF) (mice flagged for domed heads) or postfixed in 10% neutral buffered formalin (mice found dead). Heads were decalcified, paraffin-embedded in the coronal place, 10 4-µM step sections (every 50 µM) cut, stained with hematoxylin and eosin (H&E), and reviewed by a veterinary pathologist.

Brains from experimentally naïve male hemizygous mutants or KOs and male WT littermate controls were harvested at 8 weeks (hnRNPH2 R206W and KO) or 3 weeks (hnRNPH2 P209L) of age for histology and immunofluorescence. Briefly, mice were anesthetized by isoflurane inhalation and transcardially perfused with 10% NBF, the brain dissected from the skull and cut in half on the sagittal plane, processed for paraffin embedding, and cut at 10 µm. Sections were stained with H&E and Luxol fast blue-cresyl violet (LFB-CV) to ascertain overall morphology and myelination. In addition, we performed IHC using antibodies against neurons (NeuN; 2367, Cell Signaling Technology), astrocytes (GFAP; Z0334, DAKO), microglia (IBA1; CP290A, BioCare Medical), and oligodendrocytes (OLIG2; ab109186, Abcam). Sections were deparaffinized, followed by heat-induced epitope retrieval (HIER) with appropriate buffer (AR9640, Leica; 950-500 or 760-107, Roche), incubation with primary antibodies, and Bond Polymer Refine Detection with DAB (DS9800, Leica), or incubation with OmniMap Rabbit HRP antibody (760-4311, Roche) and ChromoMap DAB (760-159, Roche). Lastly, sections were counterstained with hematoxylin and, if needed, post-counterstained with

bioRxiv preprint doi: https://doi.org/10.1101/2022.03.17.484791; this version posted March 19, 2022. The copyright holder for this preprint (which was not certified by peer review) is the author/funder, who has granted bioRxiv a license to display the preprint in perpetuity. It is made available under aCC-BY-NC-ND 4.0 International license.

Bluing Reagent (760-2037, Roche), before being coverslipped. Sections were reviewed by a veterinary pathologist and immunoreactivity quantified using HALO image analysis platform (Indica Labs). The number of NeuN positive cells were quantified using QuPath software (47). Briefly, the visual, somatosensory, and somatomotor cortex was manually annotated according to the Allen mouse brain atlas, and QuPath's positive cell detection function applied. The number of NeuN positive neurons were expressed in terms of density per mm^2.

To assess the expression of hnRNPH2, immunofluorescence was performed using an N-terminal hnRNPH2 antibody (ab179439, Abcam) or a C-terminal hnRNPH2 antibody (ab181171, Abcam), as well as antibodies for neuronal nuclei (NeuN; ab104224, Abcam), or neuronal cytoplasm and processes (beta III Tubulin; ab78078, Abcam). To assess cortical cytoarchitecture, immunofluorescence was performed using antibodies against SATB2 (sc-81376, Santa Cruz Biotechnologies), which is broadly expressed in upper layer (II-IV) neurons as well as in subpopulations of deep layer (V-VI) neurons, CTIP2 (ab18465, Abcam), which is expressed exclusively in a subpopulation of layer V neurons, and FOXP2 (HPA000382, Atlas Antibodies), which is expressed in layer VI neurons. Sections were deparaffinized, followed by HIER using Universal Antigen Retrieval Reagent (Roche, CTS015), permeabilization in PBS containing 2% Triton X-100, and treatment with TrueBlack lipofuscin autofluorescence quencher (23007, Biotium). Thereafter, slides were blocked in PBS containing 4% bovine serum albumin (A2153, Sigma-Aldrich) and 2% normal goat serum (S-1000, Vector Laboratories), and incubated with primary antibodies and species-specific Alexa Fluor secondary antibodies (A32732A11029, A21434, and A21244, Thermo Fisher Scientific). Finally, slides were coverslipped with anti-fade mounting media containing DAPI (P36931, Thermo Fisher Scientific). Fluorescence slide scanning was performed using a Zeiss Axio Scan.Z1 with a Hamamatsu ORCA-Flash4.0 V3 camera using Zeiss ZEN 3.1 software. Images were created with a Zeiss Plan-Apochromat 20X/0.8 objective lens with illumination by Zeiss Colibri.2 LEDs (365 nm, 470 nm, 555 nm) and corresponding filters (Zeiss Filter Set 49, 38 HE, and 43 HE, respectively). For subcellular localization of mutant hnRNPH2, fluorescent imaging was performed using a Yokogawa CSU W1 spinning disk attached to a Nikon Ti2 eclipse with a Photometrics Prime 95B camera using Nikon Elements software. A 60× Plan Apo 1.40NA oil objective was used and Perfect Focus 2.0 (Nikon) was engaged for all captures. Imaging was performed using 405-nm, 488-nm, and 561-nm lasers for DAPI, Alexa488, and Alexa555, respectively. Image J/Fiji software (48) was used for maximum intensity Z-projection and color image processing (LUT Fire) for visualization of cytoplasmic hnRNPH2 signal. For cortical cytoarchitecture, fluorescently labeled cells were quantified using QuPath software (47). Briefly,

bioRxiv preprint doi: https://doi.org/10.1101/2022.03.17.484791; this version posted March 19, 2022. The copyright holder for this preprint (which was not certified by peer review) is the author/funder, who has granted bioRxiv a license to display the preprint in perpetuity. It is made available under aCC-BY-NC-ND 4.0 International license.

rectangular regions of interest were positioned over visual, somatosensory, and somatomotor cortical regions, with each region of interest subdivided into eight equal bins from the pia to the inner border of the cortex (49). QuPath's positive cell detection function was used to detect all cells using the DAPI channel, followed by application of a single measurement classifier for the remaining channels. The distribution of neurons was expressed as the number of SATB2, CTIP2, and FOXP2 neurons as a percentage of the total number of DAPI-positive cells within each bin.

Mouse In Situ Hybridization

Whole embryos and brains of WT C57BL/6J mice were harvested at embryonic day 12.5, 14.5, 16.5 and postnatal day 0, 7, 14, and 56, respectively. Samples were fixed in 10% neutral buffered formalin and in situ hybridization performed with a chromogenic (Fast Red), single-plex BaseScope assay (Advanced Cell Diagnostics) according to the manufacturer's instructions with custom probes against *Hnrnph1* (BA-Mm-Hnrnph1-3zz-st) and *Hnrnph2* (BA-Mm-Hnrnph2-2zz-st). Slides were scanned on the PANNORAMIC 250 Flash digital scanner (3DHISTECH) and analyzed using HALO image analysis platform according to the RNAscope quantification protocol (Indica Labs). Briefly, cells in a tissue section were grouped into 5 bins based on the number of dots per cell ranging from 0+ to 4+. Clusters were divided by the typical probe signal area to calculate a dot number for the cluster in identified cells of interest. Each sample was evaluated for the percentage of cells in each bin. The H-score for the sample was calculated by totaling the percentage of cells in each bin according to the weighted formula shown below, and a single score was assigned to an entire tissue section based on the average target expression in this tissue. H-scores were provided on a weighted scale of 0–400. The H-score was calculated using the algorithm with the following equation: H-Score = (1 × % $Probe$ 1 + $Cells$) + (2 × % $Probe$ 2 + $Cells$) + (3 × % $Probe$ 3 + $Cells$) + (4 × % $Probe$ 4 + $Cells$).

Mouse Western Blots and Digital Droplet RT-PCR

Brains from experimentally naïve male hemizygous mutants or KOs and male WT littermate controls were harvested at 8 weeks (hnRNPH2 R206W and KO) or 3 weeks (hnRNP2 P209L) of age for western blots and ddRT-PCR. In addition, brains of WT C57BL/6J mice were harvested at embryonic day 12.5, 14.5, 16.5 and postnatal day 0, 7, 14, and 56. Brains were removed, cortices dissected out, flash frozen in liquid nitrogen, and stored at -80°C.

For western blots, samples were subjected to sequential solubility fractionation or nucleocytoplasmic fractionation as previously described (50). Protein concentrations were

bioRxiv preprint doi: https://doi.org/10.1101/2022.03.17.484791; this version posted March 19, 2022. The copyright holder for this preprint (which was not certified by peer review) is the author/funder, who has granted bioRxiv a license to display the preprint in perpetuity. It is made available under aCC-BY-NC-ND 4.0 International license.

determined by DC protein assay (5000111, Bio-Rad), and 35 µg RIPA-soluble, 80 µg cytoplasmic protein, or maximum volume nuclear lysate (40 µl) was loaded onto the gel. Electrophoresis was performed using the Bolt Bis-Tris Plus mini gel system (Thermo Fisher Scientific). Gels were transferred to PVDF membranes using the iBlot 2 dry blotting system (Thermo Fisher Scientific), blocked in Odyssey TBS blocking buffer (Li-Cor), incubated with primary antibodies against hnRNPH2 (ab179439, Abcam), hnRNPH1 (PA5-50678, Thermo Fisher Scientific), GAPDH (97166, Cell Signaling Technology), or lamin A/C (Cell Signaling Technology, 2032), followed by species-specific IRDye secondary antibodies (925-3221, 925-68070, Li-Cor). Blots were imaged on the Odyssey CLx system and analyzed on Image Studio software (Li-Cor).

For ddRT-PCR, samples were treated with RNA*later*-ICE (Thermo Fisher Scientific), RNA extracted using the RNeasy Plus Universal Mini Kit (73404, Qiagen), and treated for DNA contamination with the TURBO DNA-free kit (AM1907, Thermo Fisher Scientific). 10 ng RNA was used with a one-step RT-ddPCR advanced kit for probes (1864021, Bio-Rad), together with the following assays: Mouse *Gapdh* Primer Limited (Mm99999915_g1, Thermo Fisher Scientific), Mouse *Rpp30* (dMmuCPE5097025, Bio-Rad), Mouse *Hnrnph1* (Mm00517601_m1, Thermo Fisher Scientific), and Mouse *Hnrnph2* (Mm01340844_g1, Thermo Fisher Scientific).

Statistics

Significant differences from expected Mendelian inheritance ratios were determined by chi-square tests. The log-rank (Mantel-Cox) test was used to determine significant differences between survival curves. Differences in body weight over time were determined by fitting a mixed-effects model (REML) for time, genotype, and time x genotype interaction, followed by Sidak's multiple comparisons test to compare WT mice to mutants or KOs. For differences in linear craniofacial measurements, we used a two-way ANOVA (line, genotype, line x genotype interaction), followed by Sidak's multiple comparisons test to compare WT mice to mutants or KOs. For MRI analysis and linear interlandmark distance analysis, Wilcoxon rank sum test was used to compare groups. In the EDMA analysis, biological shapes were compared using an EDMA bootstrap test (22). The global test is based on the pairwise distances in the form matrices, taking the max/min ratio of the distances. This is then done for all the B replicates, which provides the null distribution. The analysis was performed using the R package EDMAinR. Correction for multiple testing was performed using the FDR method. Significance for the incidence of hydrocephalus was determined by Fisher’s exact test. SHIRPA and audiogenic seizure scores were analyzed by aligned ranks transformation (ART) non-parametric two-way

bioRxiv preprint doi: https://doi.org/10.1101/2022.03.17.484791; this version posted March 19, 2022. The copyright holder for this preprint (which was not certified by peer review) is the author/funder, who has granted bioRxiv a license to display the preprint in perpetuity. It is made available under aCC-BY-NC-ND 4.0 International license.

ANOVA (line, genotype, line x genotype interaction), followed by Mann-Whitney U test to compare WT mice to mutants or KOs. Differences in all motor tests, optomotor response, and hot plate test were determined by two-way ANOVA (line, genotype, line x genotype interaction) followed by Sidak's multiple comparisons test to compare WT mice to mutants or KOs. Scent habituation data were analyzed by repeated measures two-way ANOVA (trial, genotype, trial x genotype interaction), followed by Sidak's multiple comparisons test to compare WT mice to mutants or KOs. Nuclear hnRNPH2 levels in mouse cortex by western blot were subjected to unpaired t tests. *Hnrnph1* and *Hnrnph2* transcript levels measured by ddRT-PCR were analyzed by two-way ANOVA (line, genotype, line x genotype interaction) followed by Sidak's multiple comparisons test to compare WT to mutants or KOs. *Hnrnph1* and *Hnrnph2* expression by ddRT-PCR and ISH were analyzed by two-way ANOVA (genotype, developmental time point, genotype x developmental time point interaction) followed by Sidak's multiple comparisons test to compare *Hnrnph1* levels to *Hnrnph2* levels at each time point, or Tukey's multiple comparisons test to compare transcript levels between developmental time points for each gene separately. *Hnrnph2* expression by ddRT-PCR in *Hnrnph2* KO mice were analyzed by one-way ANOVA followed by Sidak's multiple comparisons test to compare WT males to hemizygous KO males, as well as WT females to heterozygous and homozygous KO females. NeuN positive cell counts were analyzed by two-way ANOVA (line, genotype, line x genotype interaction) followed by Sidak's multiple comparisons test to compare WT to mutants or KOs. For cortical layer analysis, the % of SATB2, CTIP2 and FOXP2 positive neurons were analyzed by two-way ANOVA (genotype, bin, genotype x bin interaction), followed by Tukey's multiple comparisons test.

bioRxiv preprint doi: https://doi.org/10.1101/2022.03.17.484791; this version posted March 19, 2022. The copyright holder for this preprint (which was not certified by peer review) is the author/funder, who has granted bioRxiv a license to display the preprint in perpetuity. It is made available under aCC-BY-NC-ND 4.0 International license.

References

1. Bain JM, Cho MT, Telegrafi A, Wilson A, Brooks S, Botti C, et al. Variants in HNRNPH2 on the X Chromosome Are Associated with a Neurodevelopmental Disorder in Females. *Am J Hum Genet.* 2016;99(3):728-34.
2. Bain JM, Thornburg O, Pan C, Rome-Martin D, Boyle L, Fan X, et al. Detailed Clinical and Psychological Phenotype of the X-linked HNRNPH2-Related Neurodevelopmental Disorder. *Neurol Genet.* 2021;7(1):e551.
3. White-Brown AM, Lemire G, Ito YA, Thornburg O, Bain JM, and Dyment DA. A disease-causing variant in HNRNPH2 inherited from an unaffected mother with skewed X-inactivation. *Am J Med Genet A.* 2022;188(2):668-71.
4. Kreienkamp HJ, Wagner M, Weigand H, McConkie-Rossell A, McDonald M, Keren B, et al. Variant-specific effects define the phenotypic spectrum of HNRNPH2-associated neurodevelopmental disorders in males. *Hum Genet.* 2022;141(2):257-72.
5. Somashekar PH, Narayanan DL, Jagadeesh S, Suresh B, Vaishnavi RD, Bielas S, et al. Bain type of X-linked syndromic mental retardation in a male with a pathogenic variant in HNRNPH2. *Am J Med Genet A.* 2020;182(1):183-8.
6. Harmsen S, Buchert R, Mayatepek E, Haack TB, and Distelmaier F. Bain type of X-linked syndromic mental retardation in boys. *Clin Genet.* 2019;95(6):734-5.
7. Jepsen WM, Ramsey K, Szelinger S, Llaci L, Balak C, Belnap N, et al. Two additional males with X-linked, syndromic mental retardation carry de novo mutations in HNRNPH2. *Clin Genet.* 2019;96(2):183-5.
8. Kreienkamp HJ, Wagner M, Weigand H, McConkie-Rossell A, McDonald M, Keren B, et al. Variant-specific effects define the phenotypic spectrum of HNRNPH2-associated neurodevelopmental disorders in males. *Hum Genet.* 2021.
9. Salazar R, Beenders S, LaMarca NM, Thornburg O, Rubin-Thompson L, Snow A, et al. Cross-sectional, quantitative analysis of motor function in females with HNRNPH2-related disorder. *Res Dev Disabil.* 2021;119:104110.
10. Pilch J, Koppolu AA, Walczak A, Murcia Pienkowski VA, Biernacka A, Skiba P, et al. Evidence for HNRNPH1 being another gene for Bain type syndromic mental retardation. *Clin Genet.* 2018;94(3-4):381-5.
11. Reichert SC, Li R, S AT, van Jaarsveld RH, Massink MPG, van den Boogaard MH, et al. HNRNPH1-related syndromic intellectual disability: Seven additional cases suggestive of a distinct syndromic neurodevelopmental syndrome. *Clin Genet.* 2020;98(1):91-8.
12. Geuens T, Bouhy D, and Timmerman V. The hnRNP family: insights into their role in health and disease. *Hum Genet.* 2016;135(8):851-67.
13. Van Dusen CM, Yee L, McNally LM, and McNally MT. A glycine-rich domain of hnRNP H/F promotes nucleocytoplasmic shuttling and nuclear import through an interaction with transportin 1. *Mol Cell Biol.* 2010;30(10):2552-62.
14. Lee BJ, Cansizoglu AE, Suel KE, Louis TH, Zhang Z, and Chook YM. Rules for nuclear localization sequence recognition by karyopherin beta 2. *Cell.* 2006;126(3):543-58.
15. Liu Q, Shu S, Wang RR, Liu F, Cui B, Guo XN, et al. Whole-exome sequencing identifies a missense mutation in hnRNPA1 in a family with flail arm ALS. *Neurology.* 2016;87(17):1763-9.
16. Naruse H, Ishiura H, Mitsui J, Date H, Takahashi Y, Matsukawa T, et al. Molecular epidemiological study of familial amyotrophic lateral sclerosis in Japanese population by whole-exome sequencing and identification of novel HNRNPA1 mutation. *Neurobiol Aging.* 2018;61:255 e9- e16.
17. Dormann D, Rodde R, Edbauer D, Bentmann E, Fischer I, Hruscha A, et al. ALS-associated fused in sarcoma (FUS) mutations disrupt Transportin-mediated nuclear import. *EMBO J.* 2010;29(16):2841-57.

bioRxiv preprint doi: https://doi.org/10.1101/2022.03.17.484791; this version posted March 19, 2022. The copyright holder for this preprint (which was not certified by peer review) is the author/funder, who has granted bioRxiv a license to display the preprint in perpetuity. It is made available under aCC-BY-NC-ND 4.0 International license.

18. Siomi MC, Eder PS, Kataoka N, Wan L, Liu Q, and Dreyfuss G. Transportin-mediated nuclear import of heterogeneous nuclear RNP proteins. *J Cell Biol.* 1997;138(6):1181-92.
19. Cansizoglu AE, Lee BJ, Zhang ZC, Fontoura BM, and Chook YM. Structure-based design of a pathway-specific nuclear import inhibitor. *Nat Struct Mol Biol.* 2007;14(5):452-4.
20. Richtsmeier JT, Baxter LL, and Reeves RH. Parallels of craniofacial maldevelopment in Down syndrome and Ts65Dn mice. *Dev Dyn.* 2000;217(2):137-45.
21. Maga AM, Tustison NJ, and Avants BB. A population level atlas of Mus musculus craniofacial skeleton and automated image-based shape analysis. *J Anat.* 2017;231(3):433-43.
22. Lele S, and Richtsmeier JT. Euclidean distance matrix analysis: a coordinate-free approach for comparing biological shapes using landmark data. *Am J Phys Anthropol.* 1991;86(3):415-27.
23. Menegaz RA, Ladd SH, and Organ JM. Craniofacial allometry in the OIM(-/-) mouse model of osteogenesis imperfecta. *FASEB J.* 2020;34(8):10850-9.
24. Hill CA, Sussan TE, Reeves RH, and Richtsmeier JT. Complex contributions of Ets2 to craniofacial and thymus phenotypes of trisomic "Down syndrome" mice. *Am J Med Genet A.* 2009;149A(10):2158-65.
25. Vogel P, Read RW, Hansen GM, Payne BJ, Small D, Sands AT, et al. Congenital hydrocephalus in genetically engineered mice. *Vet Pathol.* 2012;49(1):166-81.
26. Dorr AE, Lerch JP, Spring S, Kabani N, and Henkelman RM. High resolution three-dimensional brain atlas using an average magnetic resonance image of 40 adult C57Bl/6J mice. *Neuroimage.* 2008;42(1):60-9.
27. Gates H, Mallon AM, Brown SD, and Consortium E. High-throughput mouse phenotyping. *Methods.* 2011;53(4):394-404.
28. Rogers DC, Fisher EM, Brown SD, Peters J, Hunter AJ, and Martin JE. Behavioral and functional analysis of mouse phenotype: SHIRPA, a proposed protocol for comprehensive phenotype assessment. *Mamm Genome.* 1997;8(10):711-3.
29. Gonzalez D, Tomasek M, Hays S, Sridhar V, Ammanuel S, Chang CW, et al. Audiogenic Seizures in the Fmr1 Knock-Out Mouse Are Induced by Fmr1 Deletion in Subcortical, VGlut2-Expressing Excitatory Neurons and Require Deletion in the Inferior Colliculus. *J Neurosci.* 2019;39(49):9852-63.
30. Mandel-Brehm C, Salogiannis J, Dhamne SC, Rotenberg A, and Greenberg ME. Seizure-like activity in a juvenile Angelman syndrome mouse model is attenuated by reducing Arc expression. *Proc Natl Acad Sci U S A.* 2015;112(16):5129-34.
31. Grammatikakis I, Zhang P, Panda AC, Kim J, Maudsley S, Abdelmohsen K, et al. Alternative Splicing of Neuronal Differentiation Factor TRF2 Regulated by HNRNPH1/H2. *Cell Rep.* 2016;15(5):926-34.
32. Lein ES, Hawrylycz MJ, Ao N, Ayres M, Bensinger A, Bernard A, et al. Genome-wide atlas of gene expression in the adult mouse brain. *Nature.* 2007;445(7124):168-76.
33. Kang HJ, Kawasawa YI, Cheng F, Zhu Y, Xu X, Li M, et al. Spatio-temporal transcriptome of the human brain. *Nature.* 2011;478(7370):483-9.
34. Consortium GT, Laboratory DA, Coordinating Center -Analysis Working G, Statistical Methods groups-Analysis Working G, Enhancing Gg, Fund NIHC, et al. Genetic effects on gene expression across human tissues. *Nature.* 2017;550(7675):204-13.
35. Gordon A, Yoon SJ, Tran SS, Makinson CD, Park JY, Andersen J, et al. Long-term maturation of human cortical organoids matches key early postnatal transitions. *Nat Neurosci.* 2021;24(3):331-42.

bioRxiv preprint doi: https://doi.org/10.1101/2022.03.17.484791; this version posted March 19, 2022. The copyright holder for this preprint (which was not certified by peer review) is the author/funder, who has granted bioRxiv a license to display the preprint in perpetuity. It is made available under aCC-BY-NC-ND 4.0 International license.

36. Zhang Y, Chen K, Sloan SA, Bennett ML, Scholze AR, O'Keeffe S, et al. An RNA-sequencing transcriptome and splicing database of glia, neurons, and vascular cells of the cerebral cortex. *J Neurosci.* 2014;34(36):11929-47.
37. Zhang Y, Sloan SA, Clarke LE, Caneda C, Plaza CA, Blumenthal PD, et al. Purification and Characterization of Progenitor and Mature Human Astrocytes Reveals Transcriptional and Functional Differences with Mouse. *Neuron.* 2016;89(1):37-53.
38. Saunders A, Macosko EZ, Wysoker A, Goldman M, Krienen FM, de Rivera H, et al. Molecular Diversity and Specializations among the Cells of the Adult Mouse Brain. *Cell.* 2018;174(4):1015-30 e16.
39. Gillentine MA, Wang T, Hoekzema K, Rosenfeld J, Liu P, Guo H, et al. Rare deleterious mutations of HNRNP genes result in shared neurodevelopmental disorders. *Genome Med.* 2021;13(1):63.
40. Pletikos M, Sousa AM, Sedmak G, Meyer KA, Zhu Y, Cheng F, et al. Temporal specification and bilaterality of human neocortical topographic gene expression. *Neuron.* 2014;81(2):321-32.
41. Johnson MB, Kawasawa YI, Mason CE, Krsnik Z, Coppola G, Bogdanovic D, et al. Functional and evolutionary insights into human brain development through global transcriptome analysis. *Neuron.* 2009;62(4):494-509.
42. Hodgkins A, Farne A, Perera S, Grego T, Parry-Smith DJ, Skarnes WC, et al. WGE: a CRISPR database for genome engineering. *Bioinformatics.* 2015;31(18):3078-80.
43. Glynn D, Bortnick RA, and Morton AJ. Complexin II is essential for normal neurological function in mice. *Hum Mol Genet.* 2003;12(19):2431-48.
44. Luong TN, Carlisle HJ, Southwell A, and Patterson PH. Assessment of motor balance and coordination in mice using the balance beam. *J Vis Exp.* 2011(49).
45. Brooks SP, Trueman RC, and Dunnett SB. Assessment of Motor Coordination and Balance in Mice Using the Rotarod, Elevated Bridge, and Footprint Tests. *Curr Protoc Mouse Biol.* 2012;2(1):37-53.
46. Musumeci SA, Calabrese G, Bonaccorso CM, D'Antoni S, Brouwer JR, Bakker CE, et al. Audiogenic seizure susceptibility is reduced in fragile X knockout mice after introduction of FMR1 transgenes. *Exp Neurol.* 2007;203(1):233-40.
47. Bankhead P, Loughrey MB, Fernandez JA, Dombrowski Y, McArt DG, Dunne PD, et al. QuPath: Open source software for digital pathology image analysis. *Sci Rep.* 2017;7(1):16878.
48. Schindelin J, Arganda-Carreras I, Frise E, Kaynig V, Longair M, Pietzsch T, et al. Fiji: an open-source platform for biological-image analysis. *Nat Methods.* 2012;9(7):676-82.
49. Lee FHF, Lai TKY, Su P, and Liu F. Altered cortical Cytoarchitecture in the Fmr1 knockout mouse. *Mol Brain.* 2019;12(1):56.
50. Becker LA, Huang B, Bieri G, Ma R, Knowles DA, Jafar-Nejad P, et al. Therapeutic reduction of ataxin-2 extends lifespan and reduces pathology in TDP-43 mice. *Nature.* 2017;544(7650):367-71.

bioRxiv preprint doi: https://doi.org/10.1101/2022.03.17.484791; this version posted March 19, 2022. The copyright holder for this preprint (which was not certified by peer review) is the author/funder, who has granted bioRxiv a license to display the preprint in perpetuity. It is made available under aCC-BY-NC-ND 4.0 International license.

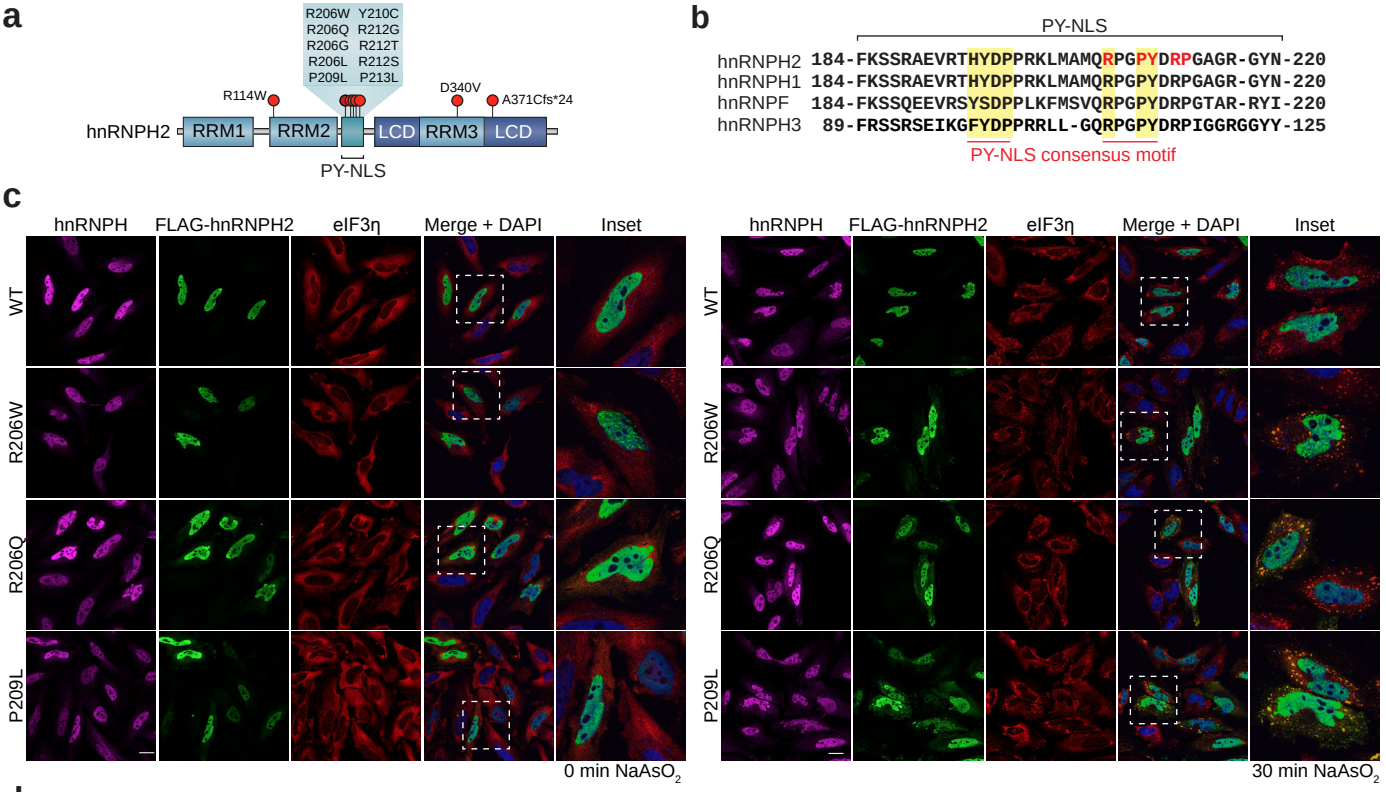

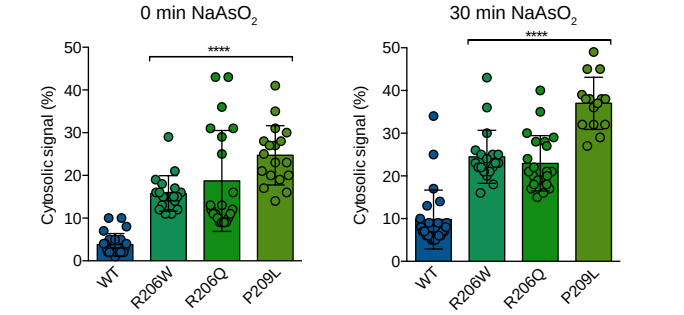

e

hnRNPH2	Cytoplasmic accumulation
WT	-
R206W	++
R206G	+++
R206Q	+++
P209L	++++
Y210C	+++
R212G	+++
R212T	+++
P213L	+
D340V	-
A371Cfs*24	-

Figure 1

bioRxiv preprint doi: https://doi.org/10.1101/2022.03.17.484791; this version posted March 19, 2022. The copyright holder for this preprint (which was not certified by peer review) is the author/funder, who has granted bioRxiv a license to display the preprint in perpetuity. It is made available under aCC-BY-NC-ND 4.0 International license.

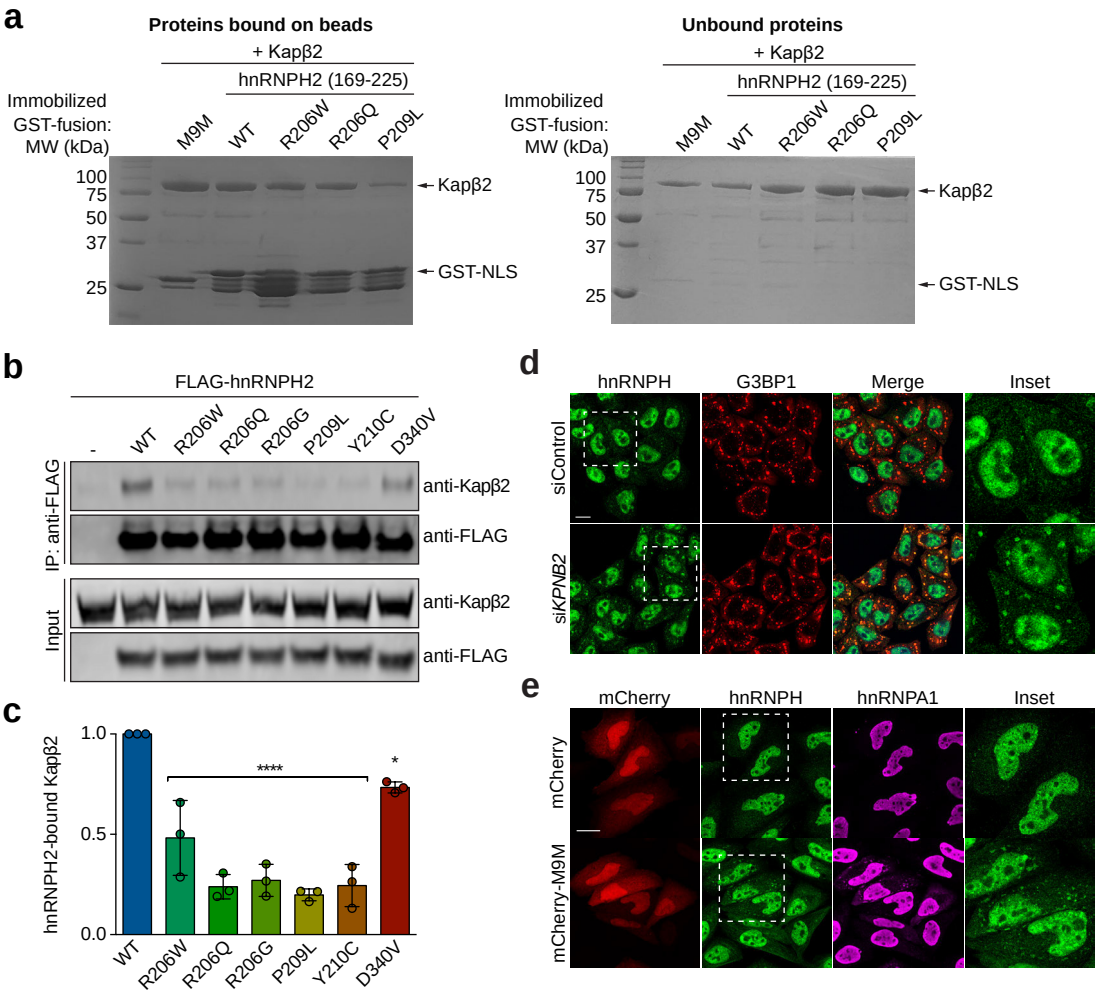

Figure 2

bioRxiv preprint doi: https://doi.org/10.1101/2022.03.17.484791; this version posted March 19, 2022. The copyright holder for this preprint (which was not certified by peer review) is the author/funder, who has granted bioRxiv a license to display the preprint in perpetuity. It is made available under aCC-BY-NC-ND 4.0 International license.

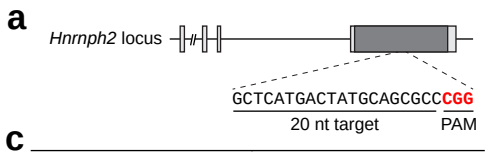

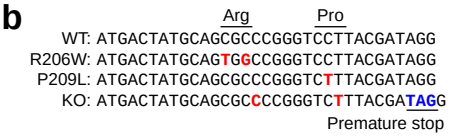

c

Males from het x WT crosses

Line	% WT (n)	% hemizygous (n)	*P*
R206W	47 (129)	53 (147)	0.279
P209L	64 (168)	36 (96)	<0.001*
KO	51 (127)	49 (124)	0.85

Females from het x WT crosses

Line	% WT (n)	% heterozygous (n)	*P*
R206W	51 (146)	49 (142)	0.814
P209L	53 (166)	47 (148)	0.31
KO	55 (145)	45 (118)	0.096

Males from het x het crosses

Line	% WT (n)	% hemizygous (n)	*P*
R206W	57 (59)	43 (40)	0.178
P209L	NA	NA	NA
KO	50 (79)	50 (80)	0.937

Females from het x het crosses

Line	% heterozygous (n)	% homozygous (n)	*P*
R206W	44 (47)	56 (59)	0.244
P209L	NA	NA	0.31
KO	53 (62)	47 (55)	0.518

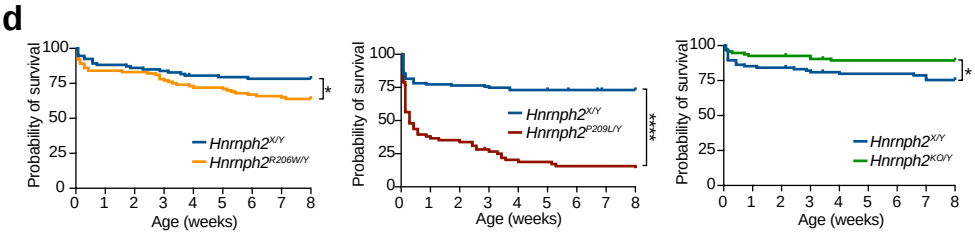

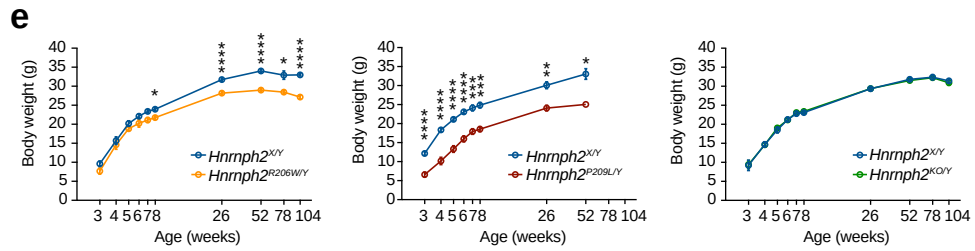

Figure 3

bioRxiv preprint doi: https://doi.org/10.1101/2022.03.17.484791; this version posted March 19, 2022. The copyright holder for this preprint (which was not certified by peer review) is the author/funder, who has granted bioRxiv a license to display the preprint in perpetuity. It is made available under aCC-BY-NC-ND 4.0 International license.

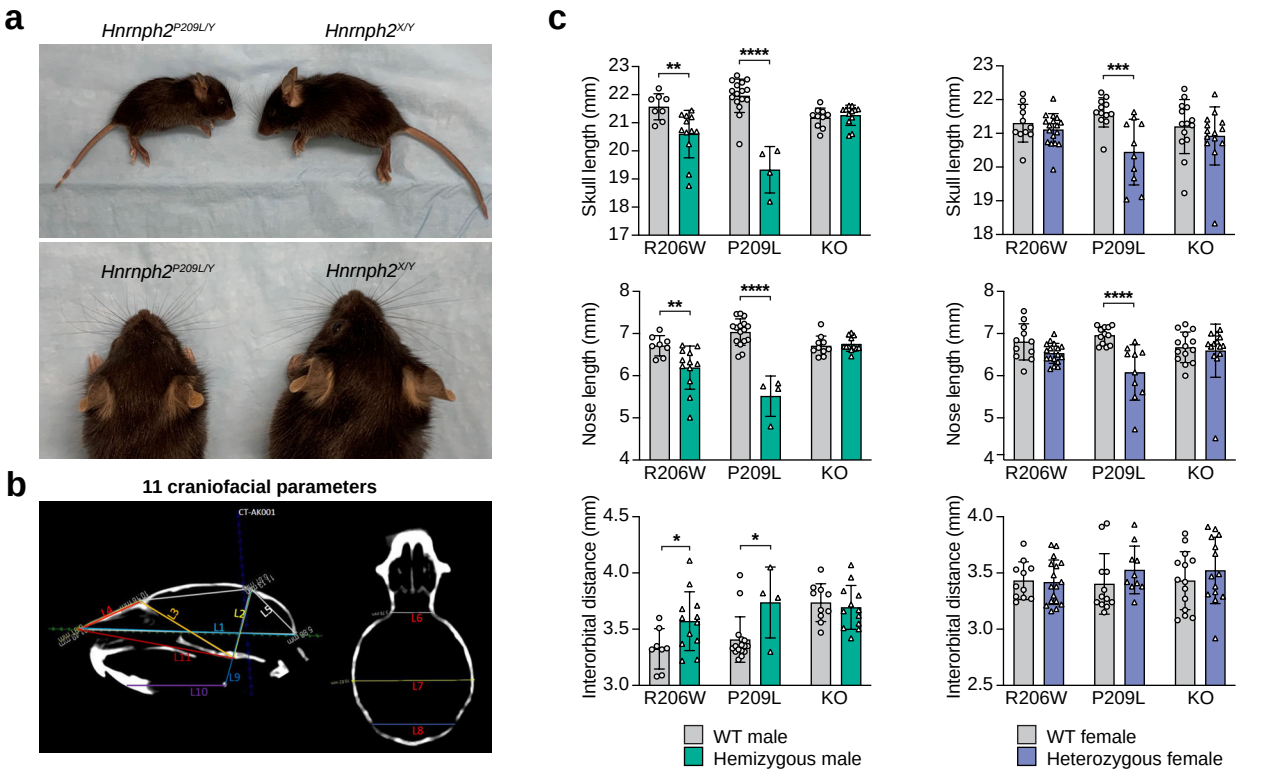

Interlandmark analysis

	Hemizygous males	Heterozygous females
Line	**Nr changed (% of total)**	**Nr changed (% of total)**
Hnrnph2 R206W	815 (63.9%)	0 (0%)
Hnrnph2 P209L	1014 (79.5%)	531 (41.6%)
Hnrnph2 KO	0 (0%)	0 (0%)

Global EDMA analysis

Line	Hemizygous males	Heterozygous females
Hnrnph2 R206W	0.029*	0.142
Hnrnph2 P209L	0.001**	0.003**
Hnrnph2 KO	0.225	0.173

Incidence of hydrocephalus: 6 weeks

	Males		Females	
Line	**WT**	**Hemizygous**	**WT**	**Heterozygous**
Hnrnph2 R206W	0/8 (0%)	4/12 (33%)	0/11 (0%)	1/17 (6%)
Hnrnph2 P209L	0/16 (0%)	3/4 (75%)**	0/12 (0%)	3/10 (30%)
Hnrnph2 KO	1/10 (10%)	1/12 (8%)	0/14 (0%)	2/14 (14%)

Incidence of hydrocephalus: 24 weeks

	Males		Females	
Line	**WT**	**Hemizygous**	**WT**	**Heterozygous**
Hnrnph2 R206W	0/8 (0%)	10/12 (83%)***	1/10 (10%)	3/17 (18%)
Hnrnph2 P209L	1/16 (6%)	3/3 (100%)**	0/12 (0%)	4/9 (44%)*
Hnrnph2 KO	1/10 (10%)	1/12 (8%)	0/14 (0%)	2/14 (14%)

Figure 4

bioRxiv preprint doi: https://doi.org/10.1101/2022.03.17.484791; this version posted March 19, 2022. The copyright holder for this preprint (which was not certified by peer review) is the author/funder, who has granted bioRxiv a license to display the preprint in perpetuity. It is made available under aCC-BY-NC-ND 4.0 International license.

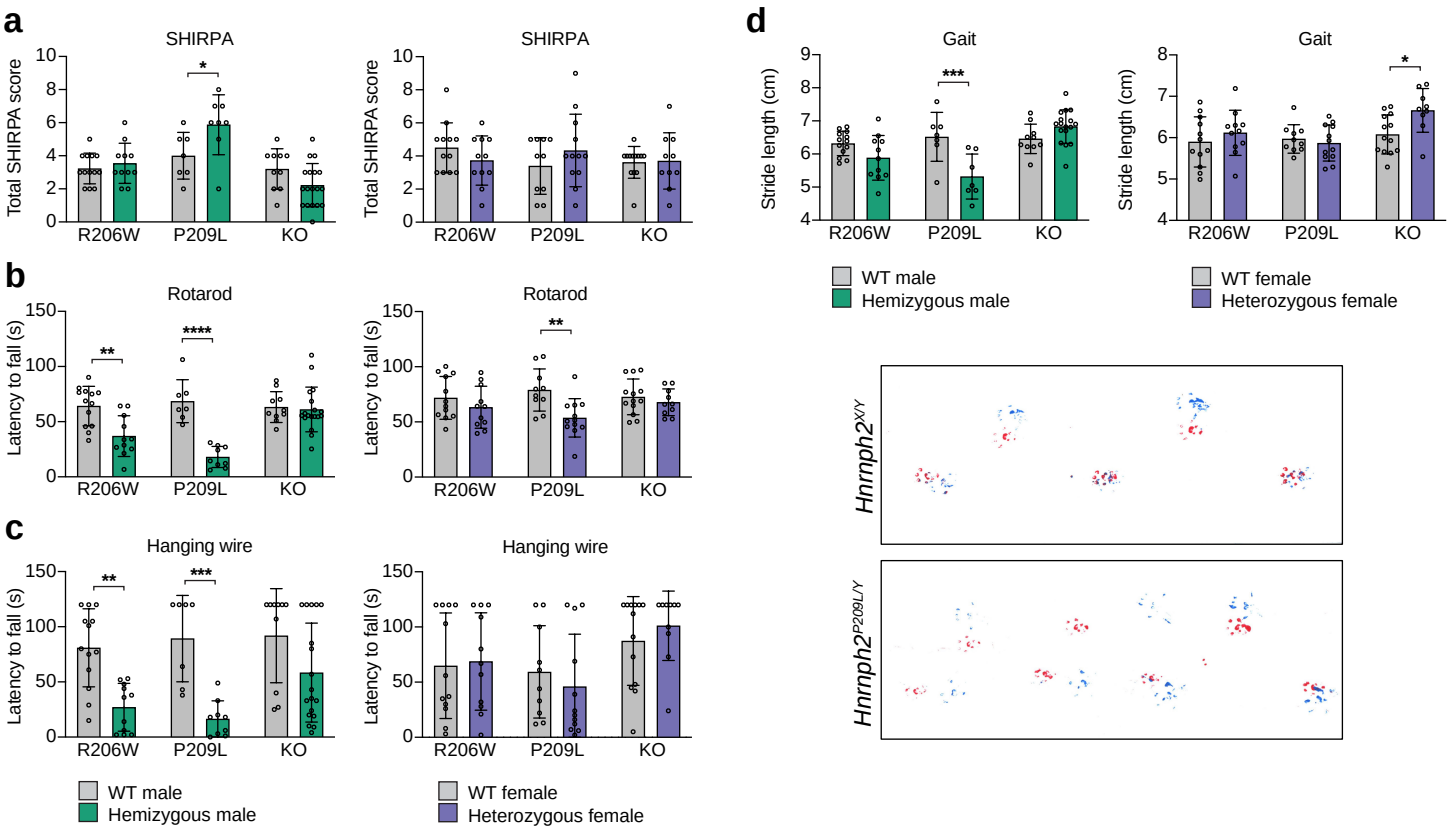

Figure 5

bioRxiv preprint doi: https://doi.org/10.1101/2022.03.17.484791; this version posted March 19, 2022. The copyright holder for this preprint (which was not certified by peer review) is the author/funder, who has granted bioRxiv a license to display the preprint in perpetuity. It is made available under aCC-BY-NC-ND 4.0 International license.

a

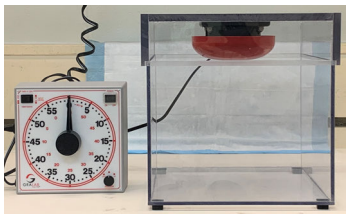

Seizure score	Behavioral expression
0	No response or slight startle
1	Wild running
2	Clonic seizures
3	Tonic seizures
4	Respiratory arrest

b

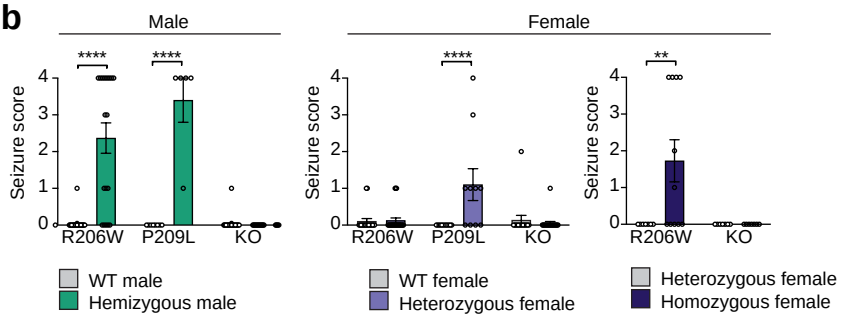

Figure 6

bioRxiv preprint doi: https://doi.org/10.1101/2022.03.17.484791; this version posted March 19, 2022. The copyright holder for this preprint (which was not certified by peer review) is the author/funder, who has granted bioRxiv a license to display the preprint in perpetuity. It is made available under aCC-BY-NC-ND 4.0 International license.

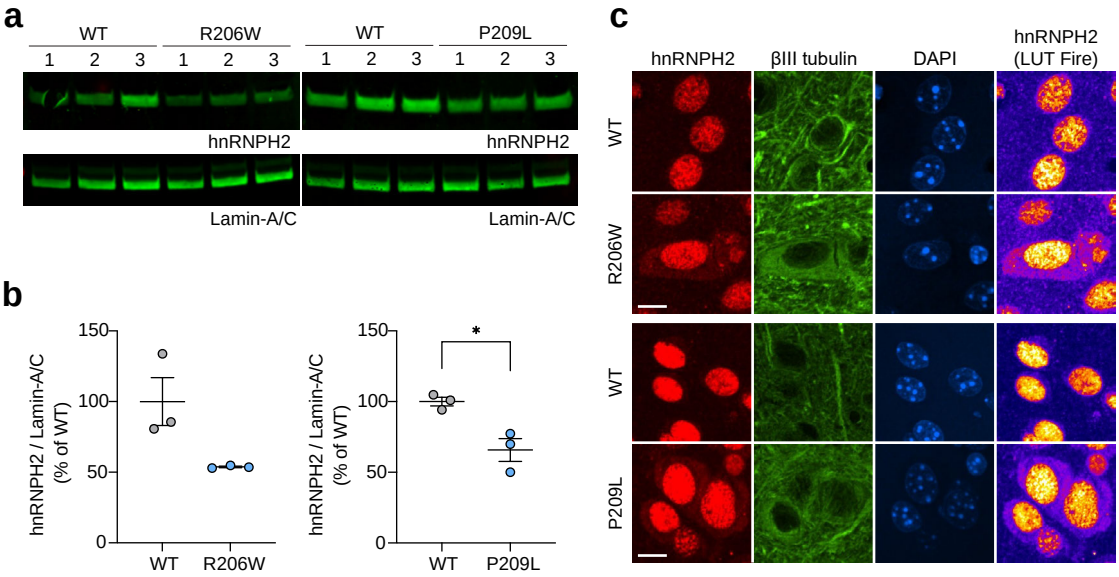

Figure 7

bioRxiv preprint doi: https://doi.org/10.1101/2022.03.17.484791; this version posted March 19, 2022. The copyright holder for this preprint (which was not certified by peer review) is the author/funder, who has granted bioRxiv a license to display the preprint in perpetuity. It is made available under aCC-BY-NC-ND 4.0 International license.

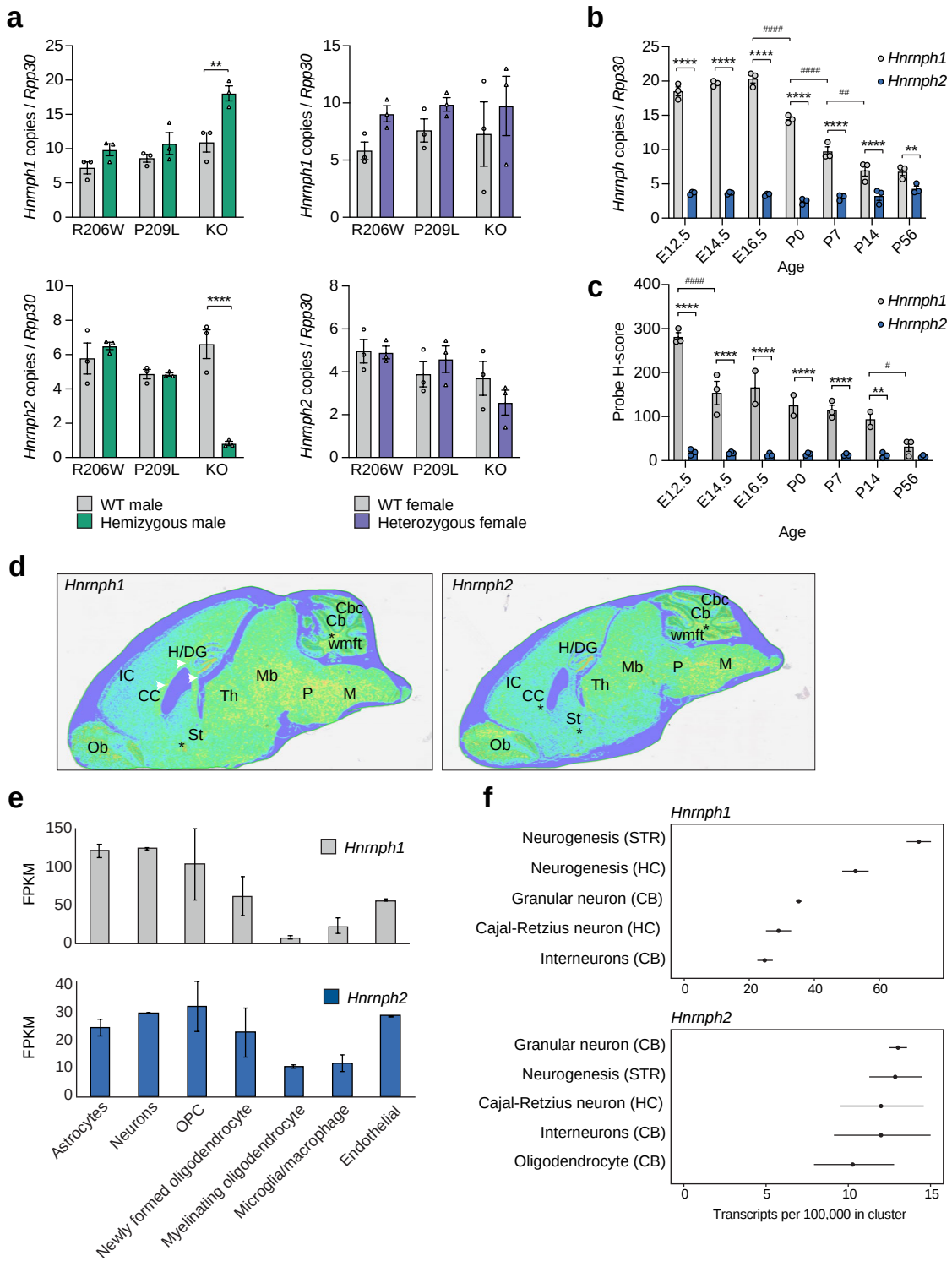

Figure 8

bioRxiv preprint doi: https://doi.org/10.1101/2022.03.17.484791; this version posted March 19, 2022. The copyright holder for this preprint (which was not certified by peer review) is the author/funder, who has granted bioRxiv a license to display the preprint in perpetuity. It is made available under aCC-BY-NC-ND 4.0 International license.

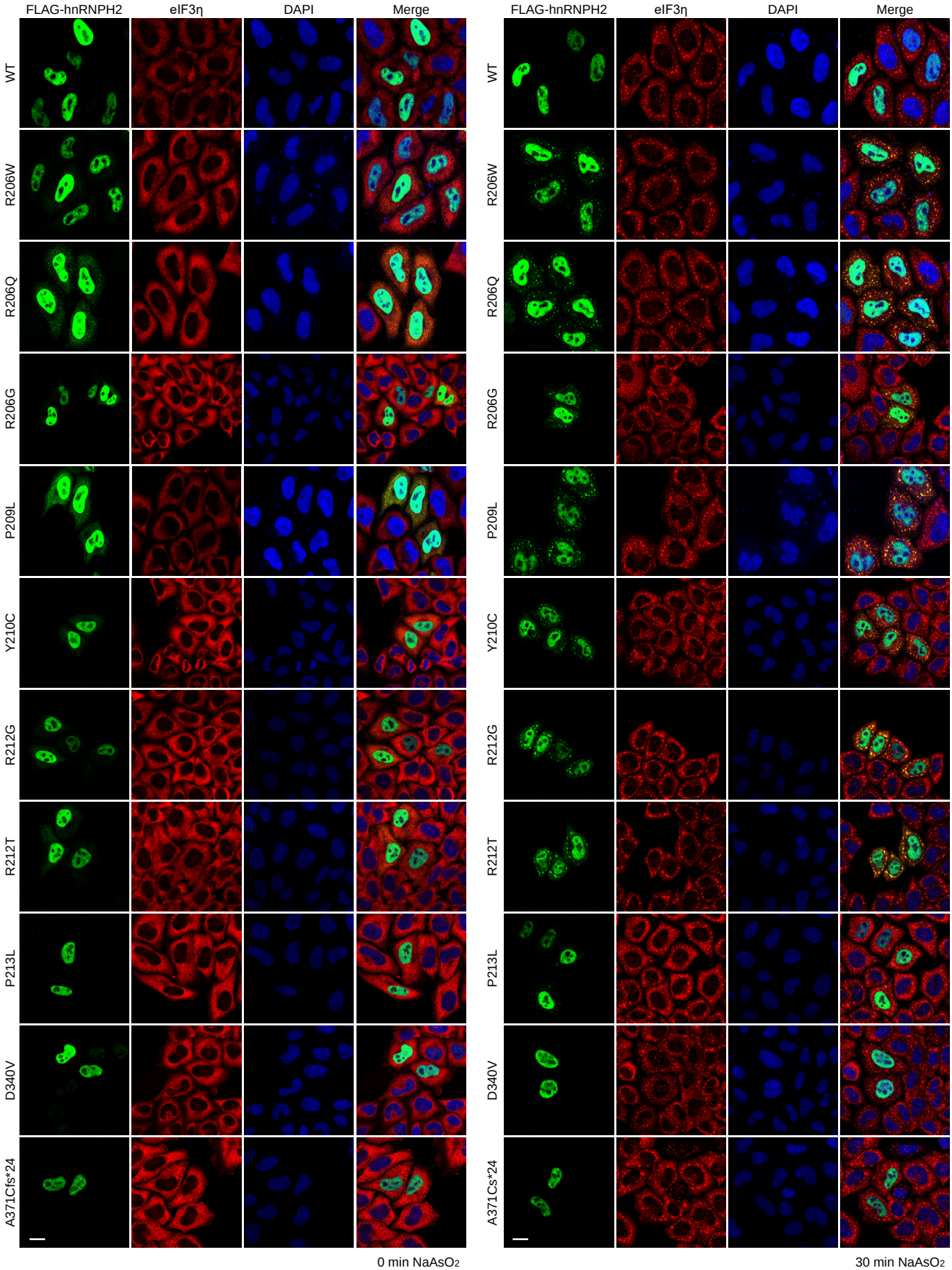

Supplementary Figure 1

bioRxiv preprint doi: https://doi.org/10.1101/2022.03.17.484791; this version posted March 19, 2022. The copyright holder for this preprint (which was not certified by peer review) is the author/funder, who has granted bioRxiv a license to display the preprint in perpetuity. It is made available under aCC-BY-NC-ND 4.0 International license.

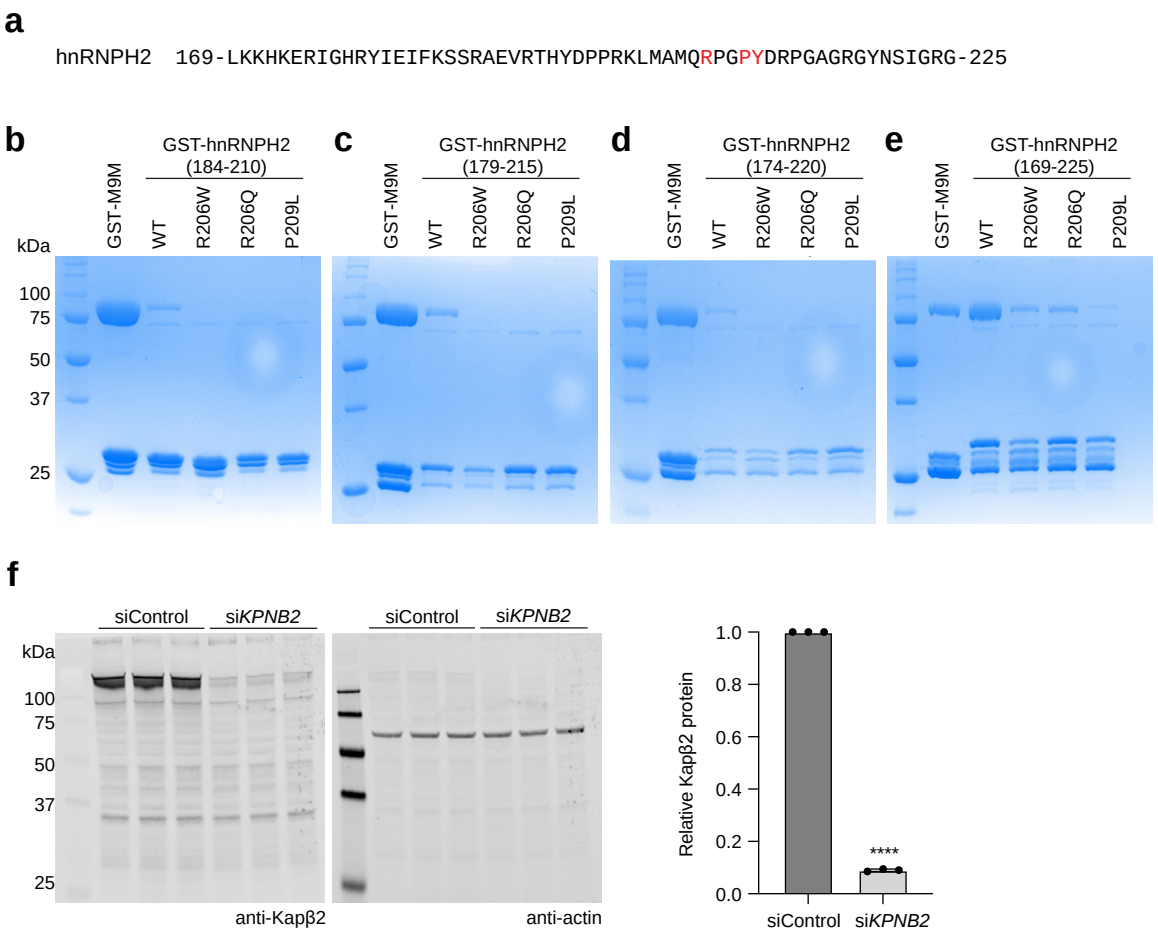

Supplementary Figure 2

bioRxiv preprint doi: https://doi.org/10.1101/2022.03.17.484791; this version posted March 19, 2022. The copyright holder for this preprint (which was not certified by peer review) is the author/funder, who has granted bioRxiv a license to display the preprint in perpetuity. It is made available under aCC-BY-NC-ND 4.0 International license.

```
sp|P55795|HNRH2_HUMAN   MMLSTEGREGFVVKVRGLPWSCSADEVMRFFSDCKIQNGTSGIRFIYTREGRPSGEAFVE 60
sp|P70333|HNRH2_MOUSE   MMLSTEGREGFVVKVRGLPWSCSAEEVMRFFSDCKIQNGTSGVRFIYTREGRPSGEAFVE 60
                        ************************:*****************:*****************

sp|P55795|HNRH2_HUMAN   LESEEEVKLALKKDRETMGHRYVEVFKSNSVEMDWVLKHTGPNSPDTANDGFVRLRGLPF 120
sp|P70333|HNRH2_MOUSE   LESEDEVKLALKKDRETMGHRYVEVFKSNSVEMDWVLKHTGPNSPDTANDGFVRLRGLPF 120
                        ****:************************************************************

sp|P55795|HNRH2_HUMAN   GCSKEEIVQFFSGLEIVPNGMTLPVDFQGRSTGEAFVQFASQEIAEKALKKHKERIGHRY 180
sp|P70333|HNRH2_MOUSE   GCSKEEIVQFFSGLEIVPNGMTLPVDFQGRSTGEAFVQFASQEIAEKALKKHKERIGHRY 180
                        ************************************************************

sp|P55795|HNRH2_HUMAN   IEIFKSSRAEVRTHYDPPRKLMAMQRPGPYDRPGAGRGYNSIGRGAGFERMRRGAYGGGY 240
sp|P70333|HNRH2_MOUSE   IEIFKSSRAEVRTHYDPPRKLMTMQRPGPYDRPGAGRGYNSIGRGAGFERMRRGAYGGGY 240
                        **********************:*************************************

sp|P55795|HNRH2_HUMAN   GGYDDYGGYNDGYGFGSDRFGRDLNYCFSGMSDHRYGDGGSSFQSTTGHCVHMRGLPYRA 300
sp|P70333|HNRH2_MOUSE   GGYDDYGGYNDGYGFGSDRFGRDLNYCFSGMSDHRYGDGGSSFQSTTGHCVHMRGLPYRA 300
                        ************************************************************

sp|P55795|HNRH2_HUMAN   TENDIYNFFSPLNPMRVHIEIGPDGRVTGEADVEFATHEDAVAAMAKDKANMQHRYVELF 360
sp|P70333|HNRH2_MOUSE   TENDIYNFFSPLNPMRVHIEIGPDGRVTGEADVEFATHEDAVAAMAKDKANMQHRYVELF 360
                        ************************************************************

sp|P55795|HNRH2_HUMAN   LNSTAGTSGGAYDHSYVELFLNSTAGASGGAYGSQMMGGMGLSNQSSYGGPASQQLSGGY 420
sp|P70333|HNRH2_MOUSE   LNSTAGTSGGAYDHSYVELFLNSTAGASGGAYGSQMMGGMGLSNQSSYGGPASQQLSGGY 420
                        ************************************************************

sp|P55795|HNRH2_HUMAN   GGGYGGQSSMSGYDQVLQENSSDYQSNLA 449
sp|P70333|HNRH2_MOUSE   GGGYGGQSSMSGYDQVLQENSSDYQSNLA 449
                        *****************************
```

Supplementary Figure 3

bioRxiv preprint doi: https://doi.org/10.1101/2022.03.17.484791; this version posted March 19, 2022. The copyright holder for this preprint (which was not certified by peer review) is the author/funder, who has granted bioRxiv a license to display the preprint in perpetuity. It is made available under aCC-BY-NC-ND 4.0 International license.

a

							R206W KI			P209L KI			KO	
Location (Mouse GRCm38)	sgRNA	Sequence	Mismatches	ID	Forward HRM primer (5' to 3')	Reverse HRM primer (5' to 3')	CFD01	CFD24	CFD27	TCF01	TCF03	TCF06	TCF02	TCF42
X:134605507-134605529	on-target	GCTCATGACTATGCAGCGCC CGG	0	original sgRNA	-	-								
8:23407852-23407874	off-target	GGTCTTGACTATGCAGTGCC TGG	3	Hnrnph2 OTsite1	CTCCCCATCCTTTGGCTCTT	CTCCTTATGCAGCAGGTAGC	WT	WT	WT	WT	WT	Variant HRM	WT	WT
4:127641881-127641903	off-target	GCCCAGGACTATGCAGGGCC AGG	3	Hnrnph2 OTsite2	TCCAAGCTCTGGTTTCTGCA	GTTCGCTGTCGATGGTTGAC	WT	WT	WT	WT	WT	Variant HRM	WT	WT
6:133972024-133972046	off-target	GTTCATGGCTATGCAGCCCC AGG	3	Hnrnph2 OTsite3	GCCTGAAGCAATGGTGAAGG	AGCTCCTGGACTTCCATGTG	WT	WT	WT	WT	WT	Variant HRM	WT	WT
3:108380888-108380910	off-target	GCGCATGACTATCCAGCTCC AGG	3	Hnrnph2 OTsite4	TACCCGTCTCAACAAGAGCC	TGTATGTGTAACTGCCTGCCT	WT	WT	WT	WT	WT	Variant HRM	WT	WT
8:15022854-15022876	off-target	GCTCTTGACTATGGAGCACC AGG	3	Hnrnph2 OTsite5	TACTGTCCTGCGTCTTCTGG	AAGACCACAAGCTCCCTGAG	WT	WT	WT	WT	WT	Variant HRM	WT	WT
5:76327518-76327540	off-target	GCTCATGACTGTGCCGCCCC TGG	3	Hnrnph2 OTsite6	ATAGCTGGCTTCCATCCACC	ATGGCAGCTTTCCCATGGA	WT	WT	WT	WT	WT	Variant HRM	WT	WT
2:106895077-106895099	off-target	GCTGATGACTATGAAGCGTC TGG	3	Hnrnph2 OTsite7	TCCAAGAAGAGGAGAAGAGGG	CCAGATTCTCGCAGCTCCTA	WT	WT	WT	WT	WT	Variant HRM	WT	WT
X:65767936-65767958	off-target	GCTTATGACTATGCAGCAGC AGG	3	Hnrnph2 OTsite8	CCACATAGTCCCAAGTGGCT	AGAGACTTGAGGGTAGAAAGGA	WT	WT	WT	WT	WT	Variant HRM	WT	WT
1:193242538-193242560	off-target	GCTCATGACTGTGCAGGGCT GGG	3	Hnrnph2 OTsite9	TGCGTGGTGGATTTCATAATGG	CCTCCCTGACAAGCCATTCT	WT	WT	WT	WT	WT	Variant HRM	WT	WT

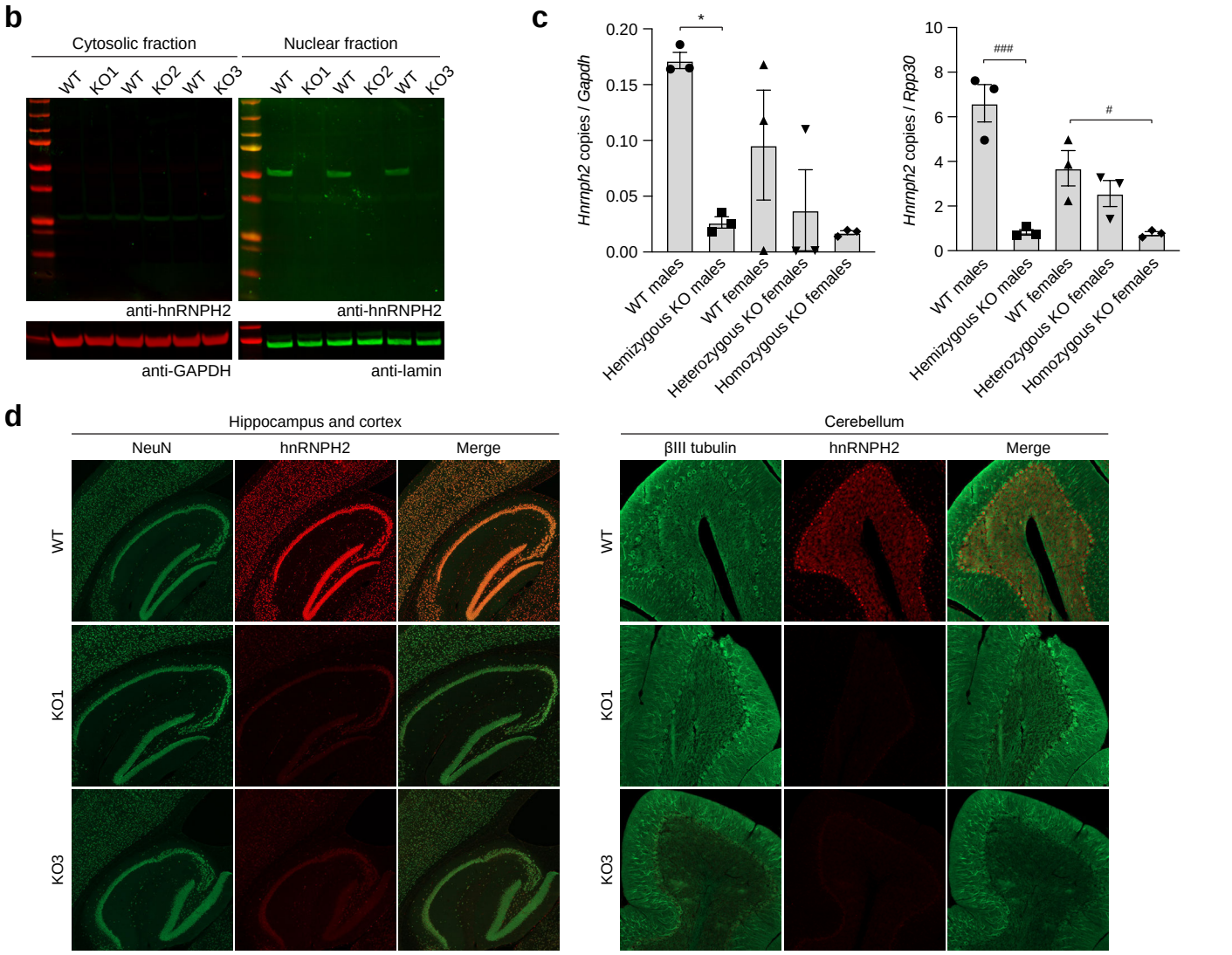

Supplementary Figure 4

bioRxiv preprint doi: https://doi.org/10.1101/2022.03.17.484791; this version posted March 19, 2022. The copyright holder for this preprint (which was not certified by peer review) is the author/funder, who has granted bioRxiv a license to display the preprint in perpetuity. It is made available under aCC-BY-NC-ND 4.0 International license.

a

Males (C57BL/6NJ-Hnrnph2$^{em1(IMPC)J}$/Mmjax)

Line	% WT (n)	% hemizygous (n)	*P*
Het x WT crosses	56 (101)	44 (80)	0.119
Het x Het crosses	55 (45)	45 (37)	0.377

Females (C57BL/6NJ-Hnrnph2$^{em1(IMPC)J}$/Mmjax)

Line	% WT (n)	% heterozygous (n)	*P*
Het x WT crosses	49 (82)	51 (86)	0.758
Line	**% heterozygous**	**% homozygous (n)**	***P***
Het x Het crosses	46 (36)	54 (42)	0.497

b

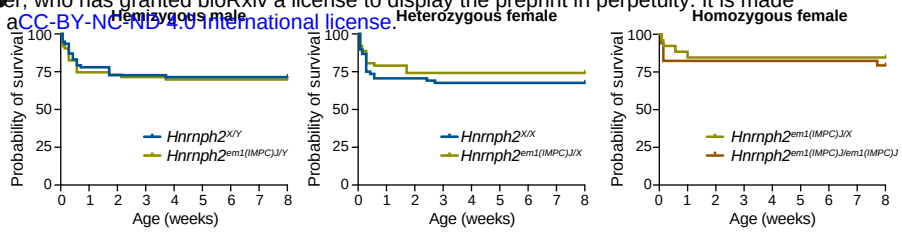

c

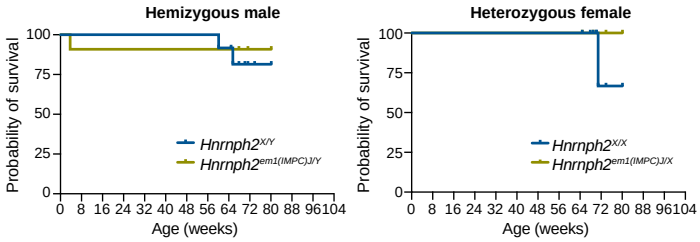

d

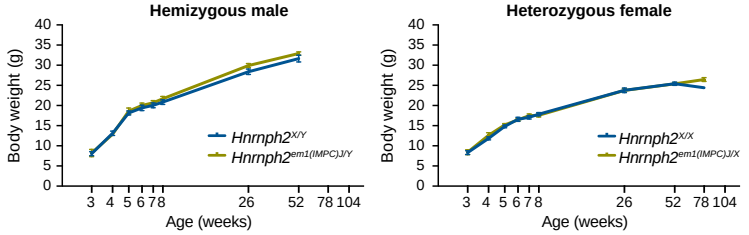

e

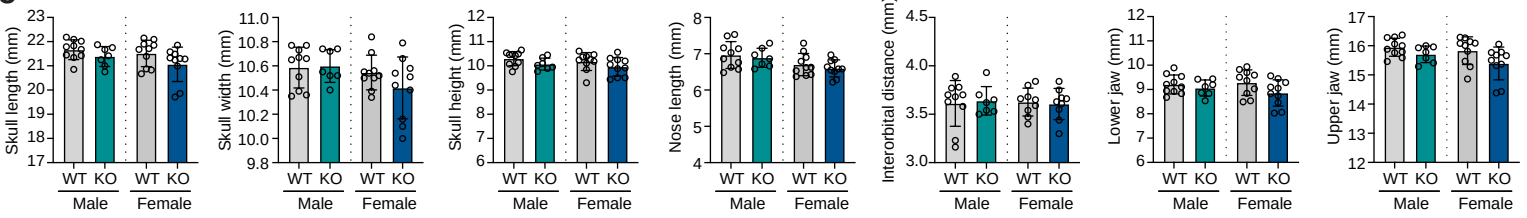

f

Interlandmark analysis

Line	Hemizygous males Nr changed (% of total)	Heterozygous females Nr changed (% of total)
Hnrnph2 KO	0 (0%)	0 (0%)

Global EDMA analysis

Line	Hemizygous males	Heterozygous females
Hnrnph2 KO	0.245	0.18

g

	Males KO	Females KO
Mesoderm derivatives	0.198	0.158
Max width of neurocranium	0.267	0.142
Midface	0.137	0.39
Neural crest - mesoderm boundary	0.102	0.017*
Neural crest derivatives	0.162	0.498
Palate	0.179	0.8
Nasal	0.102	0.481

h

Incidence of hydrocephalus

	Males		Females	
Age	**WT**	**Hemizygous**	**WT**	**Heterozygous**
6 weeks	0/10 (0%)	0/10 (0%)	0/7 (0%)	0/12 (0%)
24 weeks	0/10 (0%)	0/10 (0%)	0/10 (0%)	0/12 (0%)

i

Pathologically confirmed hydrocephalus

	Male		Female		
Line	**WT**	**Hemizygous**	**WT**	**Heterozygous**	**Homozygous**
Hnrnph2 KO	0/1	0/1	0/0	0/4	0/1

j

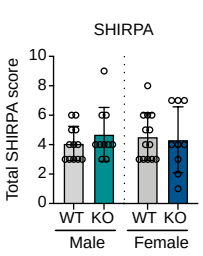

k

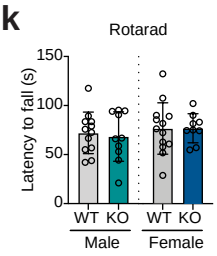

l

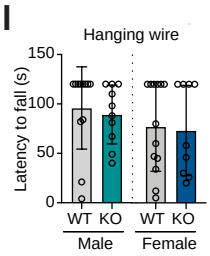

m

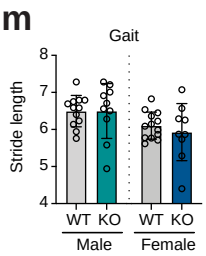

n

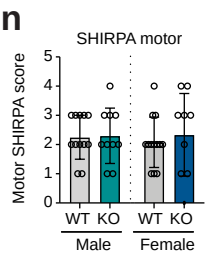

o

p

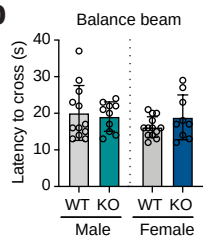

q

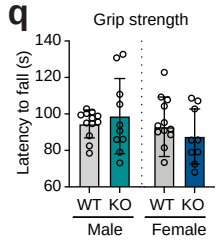

r

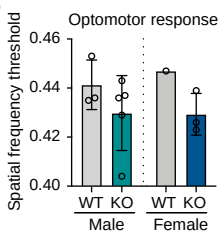

s

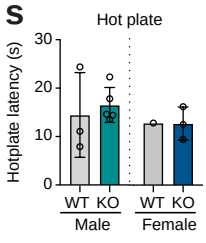

t

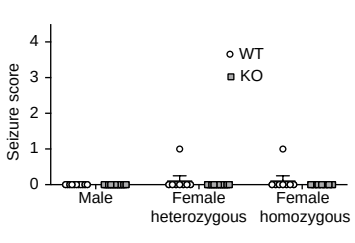

u

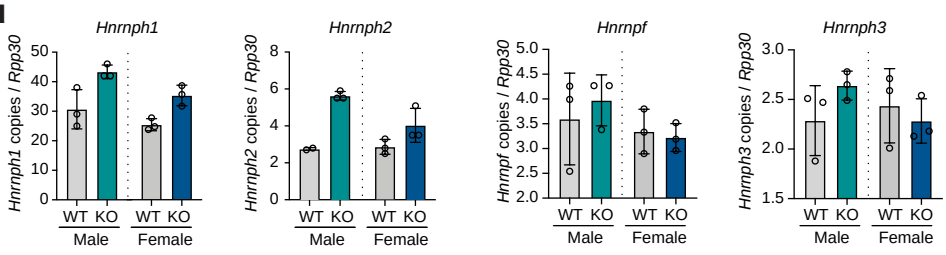

Supplementary Figure 5

bioRxiv preprint doi: https://doi.org/10.1101/2022.03.17.484791; this version posted March 19, 2022. The copyright holder for this preprint (which was not certified by peer review) is the author/funder, who has granted bioRxiv a license to display the preprint in perpetuity. It is made available under aCC-BY-NC-ND 4.0 International license.

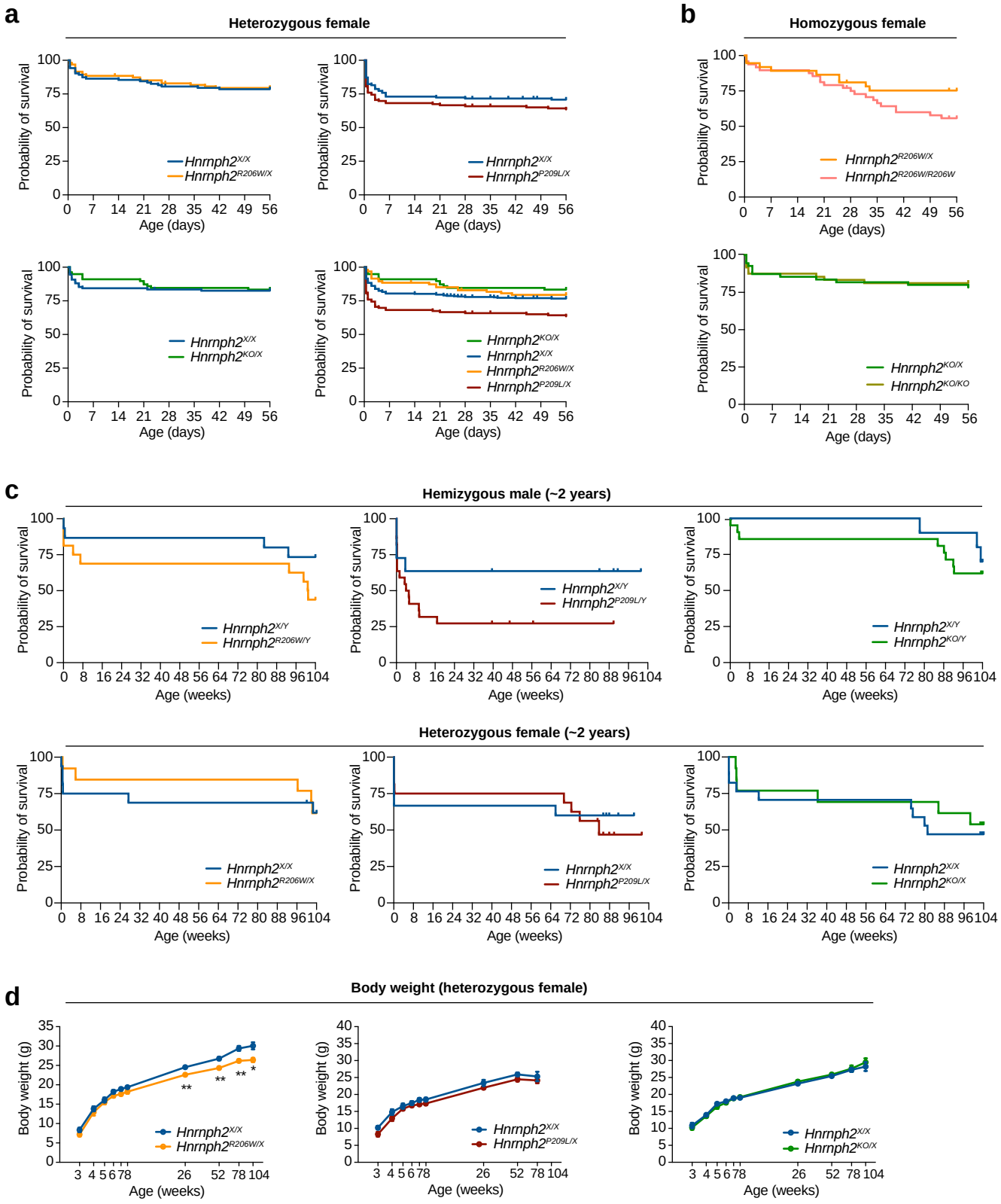

Supplementary Figure 6

bioRxiv preprint doi: https://doi.org/10.1101/2022.03.17.484791; this version posted March 19, 2022. The copyright holder for this preprint (which was not certified by peer review) is the author/funder, who has granted bioRxiv a license to display the preprint in perpetuity. It is made available under aCC-BY-NC-ND 4.0 International license.

a

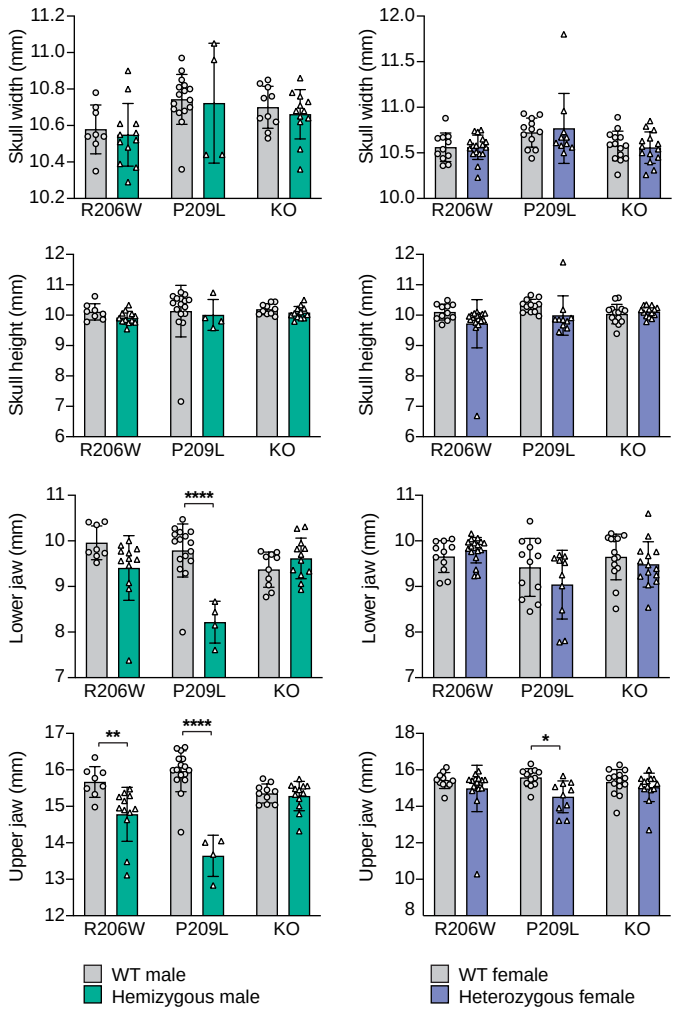

b

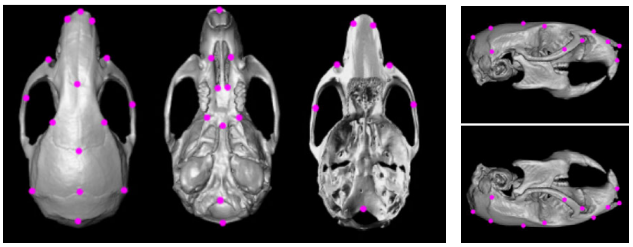

Males

	R206W	P209L	KO
Mesoderm derivatives	0.022*	0.04*	0.153
Max width of neurocranium	0.065	0.056	0.403
Midface	0.039*	<0.001***	0.342
Neural crest - Mesederm boundary	0.062	0.228	0.036*
Neural crest derivatives	0.027*	<0.001***	0.278
Palate	0.025*	0.001**	0.368
Nasal	0.084*	0.003**	0.512

Females

	R206W	P209L	KO
Mesoderm derivatives	0.062	0.018*	0.27
Max width of neurocranium	0.028*	0.135	0.12
Midface	0.026*	0.008**	0.438
Neural crest - Mesederm boundary	0.378	0.258	0.011*
Neural crest derivatives	0.029*	<0.001***	0.439
Palate	0.021*	0.035*	0.687
Nasal	0.29	0.268	0.203

c

Incidence of hydrocephalus

	Male		Female		
Line	**WT**	**Hemizygous**	**WT**	**Heterozygous**	**Homozygous**
Hnrnph2 R206W	1/2	10/16	0/0	0/1	7/10
Hnrnph2 P209L	0/1	3/6	0/0	2/6	NA
Hnrnph2 KO	2/5	0/0	0/1	0/7	0/0

d

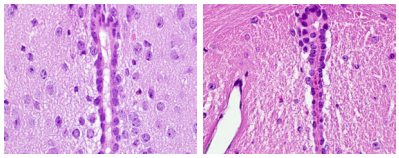

e

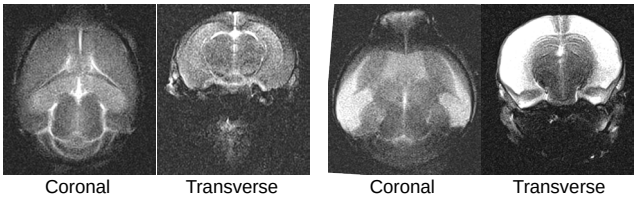

Supplementary Figure 7

bioRxiv preprint doi: https://doi.org/10.1101/2022.03.17.484791; this version posted March 19, 2022. The copyright holder for this preprint (which was not certified by peer review) is the author/funder, who has granted bioRxiv a license to display the preprint in perpetuity. It is made available under aCC-BY-NC-ND 4.0 International license.

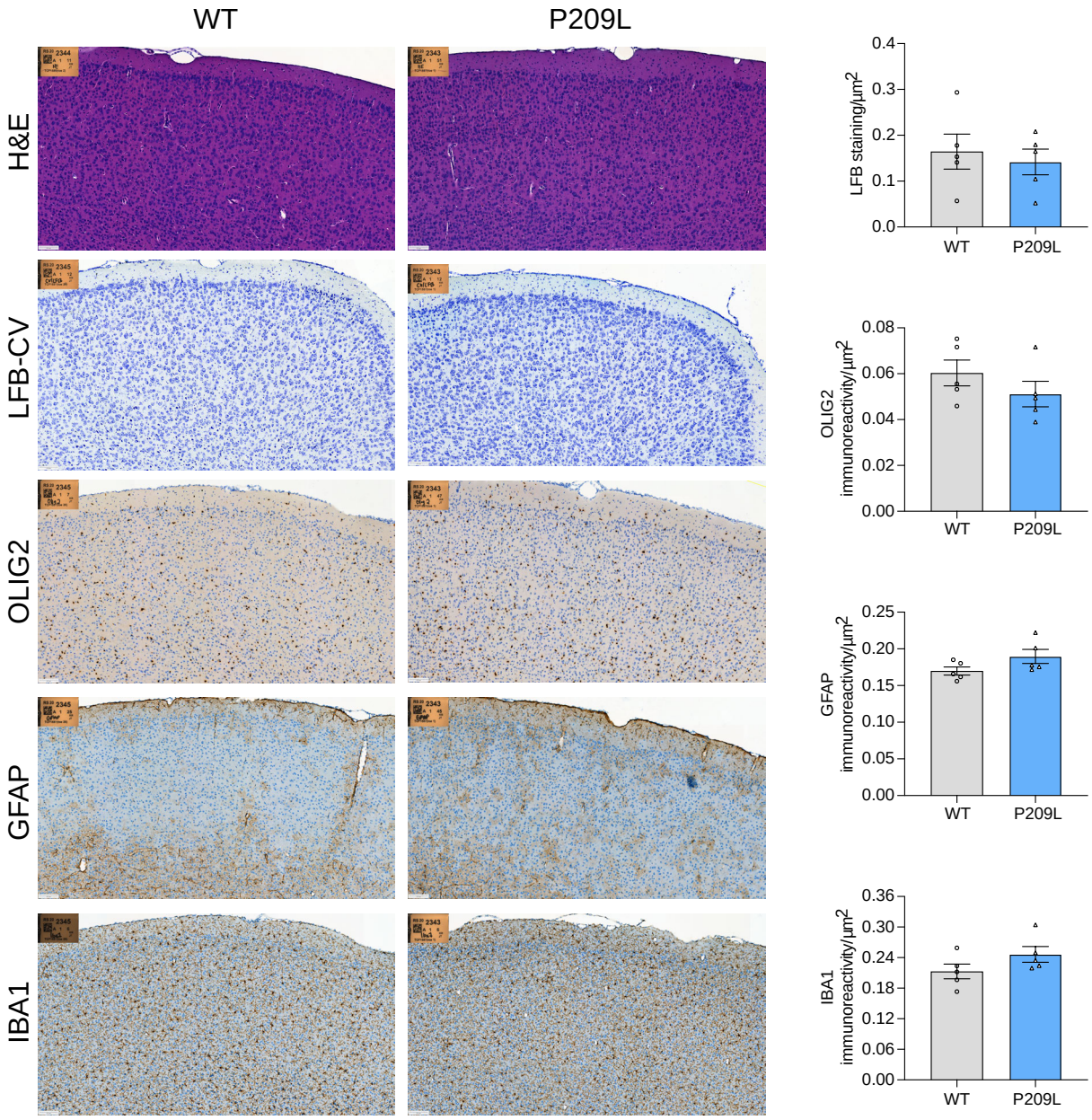

Supplementary Figure 8

bioRxiv preprint doi: https://doi.org/10.1101/2022.03.17.484791; this version posted March 19, 2022. The copyright holder for this preprint (which was not certified by peer review) is the author/funder, who has granted bioRxiv a license to display the preprint in perpetuity. It is made available under aCC-BY-NC-ND 4.0 International license.

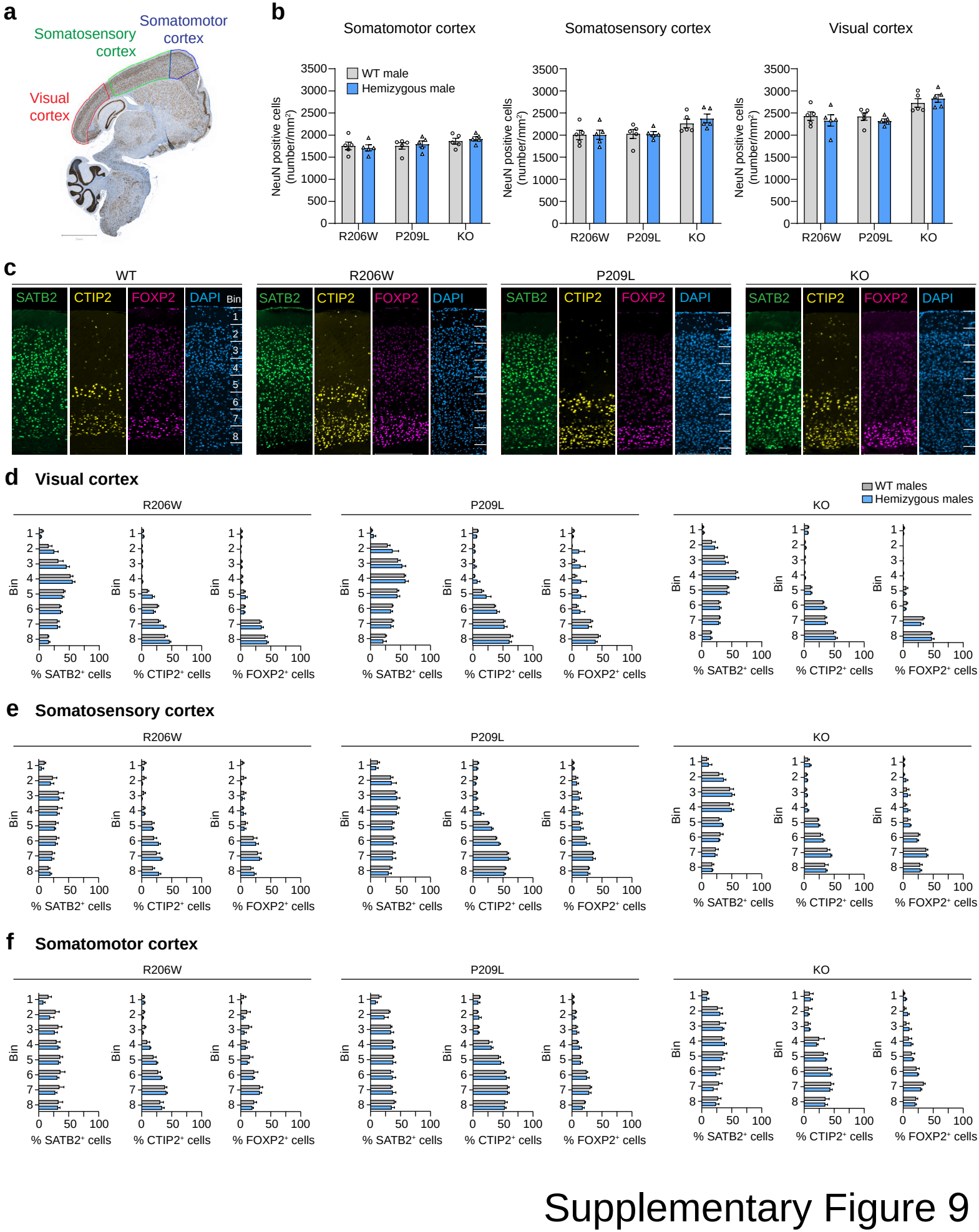

Supplementary Figure 9

bioRxiv preprint doi: https://doi.org/10.1101/2022.03.17.484791; this version posted March 19, 2022. The copyright holder for this preprint (which was not certified by peer review) is the author/funder, who has granted bioRxiv a license to display the preprint in perpetuity. It is made available under aCC-BY-NC-ND 4.0 International license.

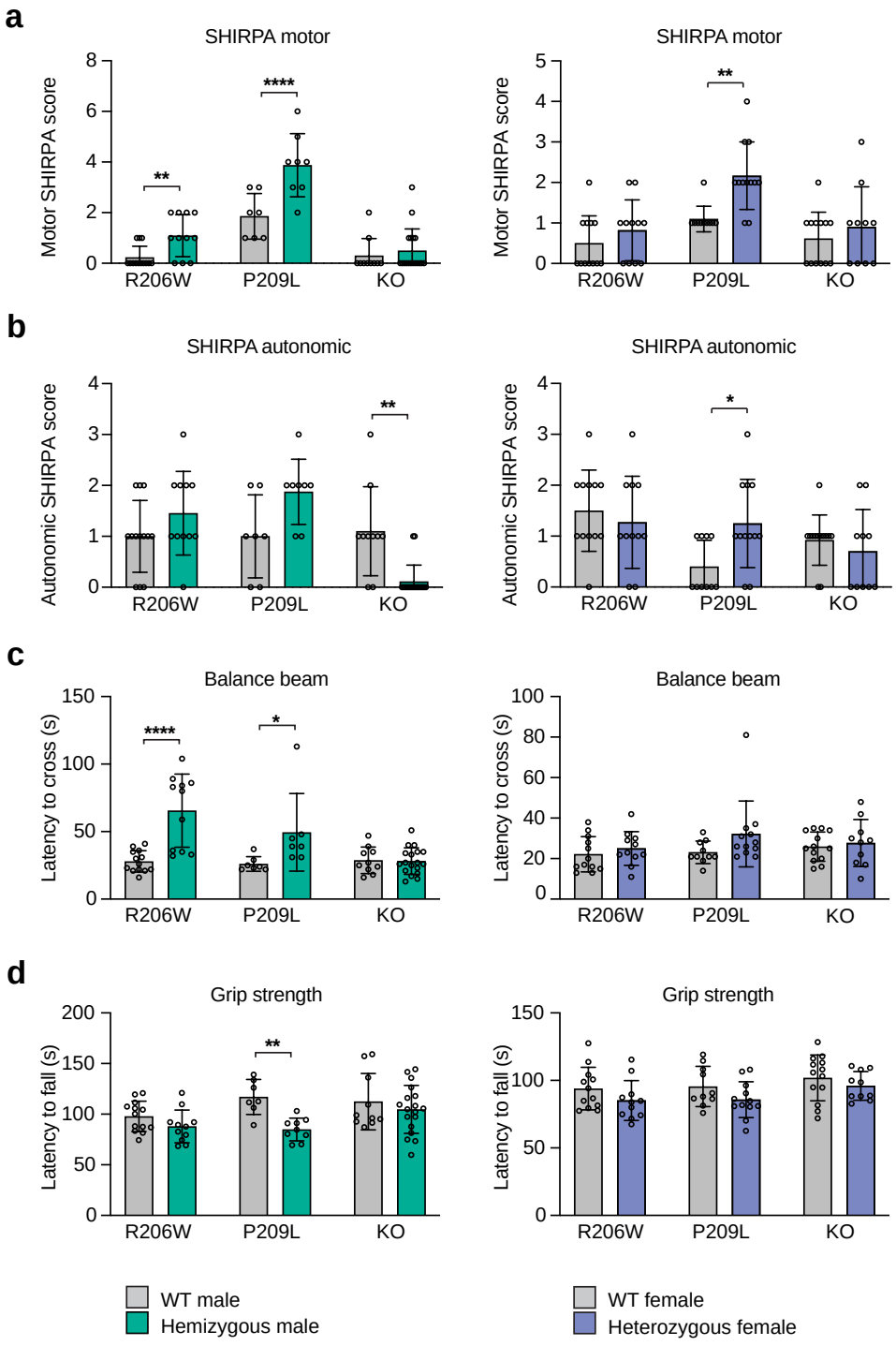

Supplementary Figure 10

bioRxiv preprint doi: https://doi.org/10.1101/2022.03.17.484791; this version posted March 19, 2022. The copyright holder for this preprint (which was not certified by peer review) is the author/funder, who has granted bioRxiv a license to display the preprint in perpetuity. It is made available under aCC-BY-NC-ND 4.0 International license.

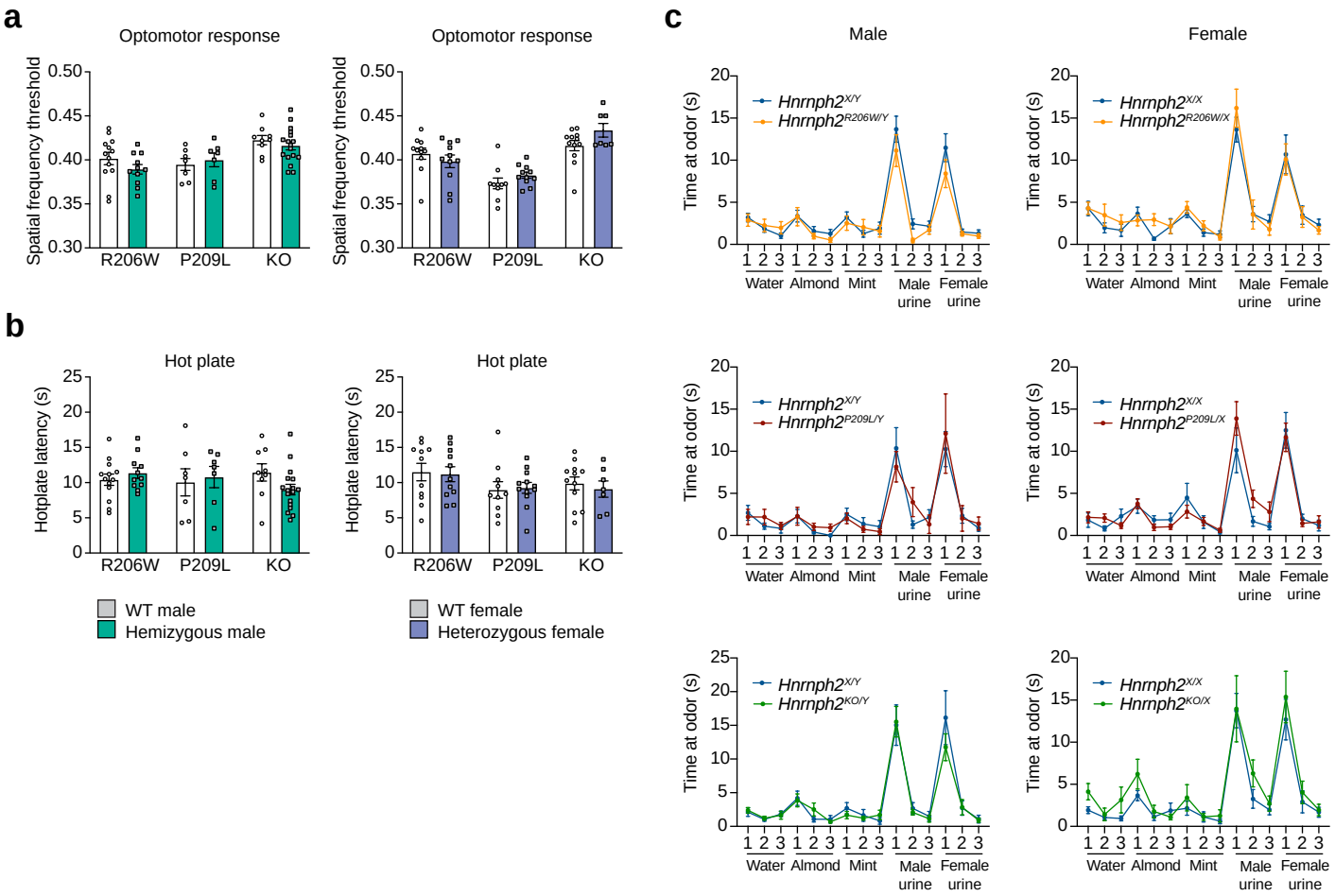

Supplementary Figure 11

bioRxiv preprint doi: https://doi.org/10.1101/2022.03.17.484791; this version posted March 19, 2022. The copyright holder for this preprint (which was not certified by peer review) is the author/funder, who has granted bioRxiv a license to display the preprint in perpetuity. It is made available under aCC-BY-NC-ND 4.0 International license.

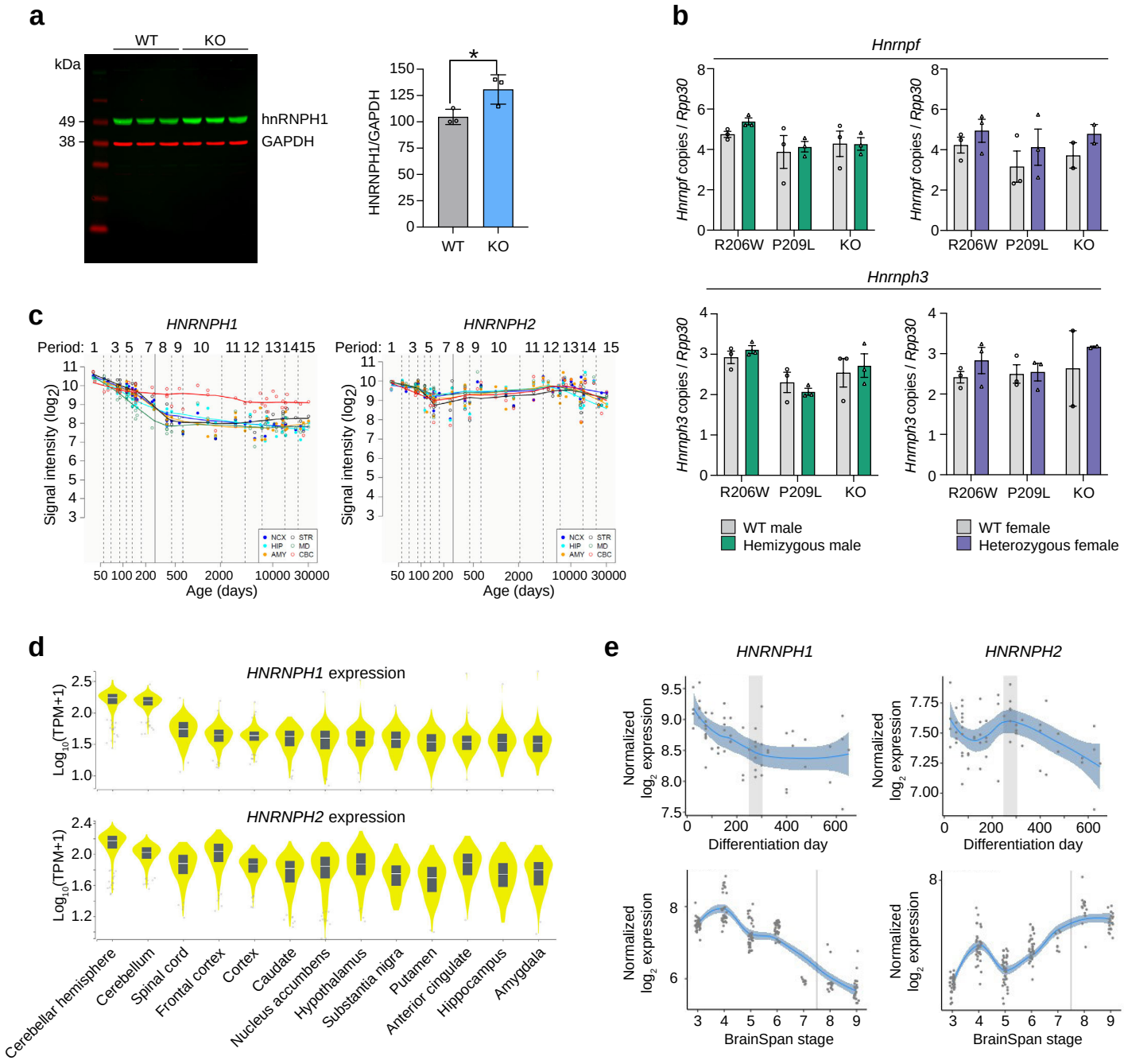

Supplementary Figure 12